A Proposal to JLab PAC 42, a companion to the WACS Proposal

Wide Angle, Exclusive Photoproduction of π^0 Mesons

J. Dunne, D. Dutta (Co-spokesperson and contact person), L. El Fassi, J. Madsen,
A Narayan, L. Ndukum, A. Subedi, L. Ye
Mississippi State University, Mississippi State, MS

P. Chu, H. Gao (Co-spokesperson), M. Huang, G. Laskaris, X. Li, M. Meziane,
C. Peng, W. Xiong, X. Yan, Z. Ye, Y. Zhang
Duke University and Triangle University Nuclear Lab, Durham, NC

J. Beričič, S. Širca (Co-spokesperson), S. Štajner
Jožef Stefan Institute and University of Ljubljana, Ljubljana, Slovenia

M. Amaryan (Co-spokesperson), C. E. Hyde, M. Kunkel (Co-spokesperson)
Old Dominion University, Norfolk, VA

W. J. Briscoe, M. U. Doering, D. Schott, I. Strakovsky (Co-spokesperson)
R. L. Workman
George Washington University, Washington, DC

A. Camsonne, S. Covrig, R. Ent, D. Gaskell, G. Gavalian, M. K. Jones, C. Keppel,
D. Mack, B. Wojtsekhowski, S. A. Wood
Jefferson Lab, Newport News, VA

I. Albayrak, M. A. Pannunzio Carmignotto, N. Hlavin, T. Horn, F. Klein,
B. Nepal, I. Sapkota
The Catholic University of America, Washington, DC

R. Lindgren
University of Virginia, Charlottesville, VA

S. Abrahamyan, A. Asaturyan, A. Mkrtchyan, H. Mkrtchyan, V. Tadevosyan,
A. Shahinyan, H. Voskanyan, S. Zhamkochyan
A.I. Alikhanyan National Science Laboratory, Yerevan, Armenia

P.M. King, J. Roche
Ohio University, Athens, OH

Nuruzzaman
Hampton University, Hampton, VA

A. Ahmidouch, S. Danagoulian
North Carolina A&T University, Greensboro, NC

M. Elassar
Southern University at New Orleans, New Orleans, LA

K. Aniol
California State University, Los Angeles, CA

M. Paolone
Temple University, Philadelphia, PA

Z. Ahmed, G. M. Huber, W. Li, D. Paudyal
University of Regina, Regina, SK, Canada

F. De Persio, F. Meddi, G. M. Urciuoli *INFN Rome and University of Rome "La Sapienza" - Rome - Italy*

E. Cisbani, F. Garibaldi *INFN Rome - Sanità Group and Italian National Institute of Health - Rome - Italy*

C. Fanelli *INFN Rome - Sanità Group and University of Rome "La Sapienza" - Rome - Italy*

A. del Dotto *Dept. of Phys. and Math. Univ. of Rome "Roma Tre" and INFN, Sezione di "Roma Tre" - Rome - Italy*

The Wide Angle Compton Scattering (WACS) collaboration

and

the Neutral Particle Spectrometer (NPS) collaboration

Hard exclusive reactions provide an excellent opportunity to study the complicated hadronic dynamics of underlying subprocesses at partonic level. The Wide Angle Compton Scattering (WACS) and exclusive photoproduction of mesons with large values of energy and momentum transfers ($s \sim t \sim u \gg \Lambda$) are among the most elementary reactions due to minimal total number of constituent partons involved in these $2 \to 2$ reactions. Existing world data on photoproduction of neutral pions on proton $\gamma + p \to \pi^0 + p$ have very large systematic errors and do not have sufficient accuracy to perform comprehensive phenomenological analysis. Preliminary expermimental data from CLAS on π^0 photoproduction extend existing world precise measurements of differential cross section up to $s \sim$11 GeV^2.

We propose to measure the differential cross section of the $\gamma p \to \pi^0 p$ process in the range of 10 GeV^2 $< s <$20 GeV^2 at large pion center-of-mass angles of $55^\circ < \theta_{cm} < 105^\circ$. The proposed measurements will be carried out in Hall C using an electron beam impinging on a 6% copper radiator and a liquid hydrogen target. The recoil proton will be detected in the HMS spectrometer and photons from the $\pi^0 \to \gamma\gamma$ decay will be detected in the Neutral Particle Spectrometer (NPS) which is under construction. The scattered electrons will be deflected by using a sweeping magnet.

This is a companion to the proposed wide angle Compton scattering (WACS) experiment. π^0 photo production differential cross section will be extracted from the same data set that is collected by the WACS experiment. In addition to all of the settings of the WACS experiment measurements at a beam energy of 6.6 GeV will be required for the proposed experiment to overlap with existing data.

CONTENTS

1. INTRODUCTION

Exclusive processes at large momentum transfers and wide angles ($p_T \geq 1GeV/c$) are essential for studies of the short range structure of nucleons. They provide a robust testing ground for QCD at intermediate energies which is one of the main goals of the physics program at JLab. Towards this goal, wide angle exclusive processes can be used to test recent developments, such as the framework based on the dominance of the "handbag mechanism" and models based on Generalized Parton Distribution (GPD) [1]. Given the relatively large cross sections for pion photoproduction, a confirmation of the dominance of the handbag mechanism would enable a study of the nucleon structure at large values of W and $-t$.

The handbag mechanism for wide-angle scattering reactions was first developed for Compton scattering [2, 3] and subsequently applied to photo- and electroproduction of mesons [4]. Several new calculations on wide-angle Compton scattering have recently become available [5–8] and they can reproduce the measured cross sections. After Compton scattering, pion photoproduction is the next simplest real photon induced exclusive process. Although calculations of the pion photoproduction cross sections tend to disagree with experiments by orders of magnitude, the charged pion ratios seem to agree with calculations at the highest energies [9]. The current situation can only be remedied with a new measurements that employs a new technique with a new high resolution and radiation hard neutral pion detector [10] along with the high luminosity that will be available at JLab Hall-C. Since the neutral pion is one of the dominant physics backgrounds for the proposed WACS experiment, this proposal uses the exact same setup and is a companion to the WACS proposal [11]. The experimental sections describing the apparatus and analysis methods and several figures used in those sections have been reproduced from the WACS proposal with the permission of the WACS spokespeople.

Wide-angle exclusive processes can also help understand the transitions from the non-perturbative to perturbative regime of QCD. The differential cross sections for many exclusive reactions [12] at high energy and large momentum transfer appear to obey the quark counting rule [13]. The quark counting rule was originally obtained based on dimensional analysis of typical renormalizable theories. The same rule was later obtained in a short-distance perturbative QCD approach by Brodsky and Lepage[14]. Despite many successes, a model-independent test of the approach, called the hadron helicity conservation rule, tends not to agree with data in the similar energy and momentum region. It has been suggested that contributions from nonzero parton orbital angular momentum could break the hadron helicity conservation rule [15], although these contributions are power suppressed [14]. In addition some of the cross-section data can also be explained in terms of non-perturbative calculations [16]. Other developments over the last decade, such as the generalized counting rule proposed by Ji *et al.* [17], the derivation of the quark-counting rule from the anti-de Sitter/Conformal Field Theory (AdS/CFT) correspondence [18], and the machinery to compute the hadronic light front wave functions developed by Brodsky *et al.* [19], have focused interest back on this subject.

Current status of experimental data on photo production of π^0 is summarized in Fig. 1 for center of mass angles $\theta = 50^\circ, 70^\circ, 90^\circ, 110^\circ$. Low energy data are from MAMI [20] (in magenta) and CLAS g1c [21] (blue points). Higher energy range measurements are preliminary CLAS data from g12 experiment [22] (red points). Data from old measurements with bremsstrahlung beams [23] (open circles) with very large systematic errors are also presented for completeness.

By fitting g12 data at $\theta = 90^\circ$ by power law function s^{-n} we obtained $n = 6.89 \pm 0.26$. The same power law function is also superimposed on data taken at $50^\circ, 70^\circ$ and 110° degrees. As one can see experimental data at lower angles tend to reach power law behavior at much higher energies. One reason for this behavior

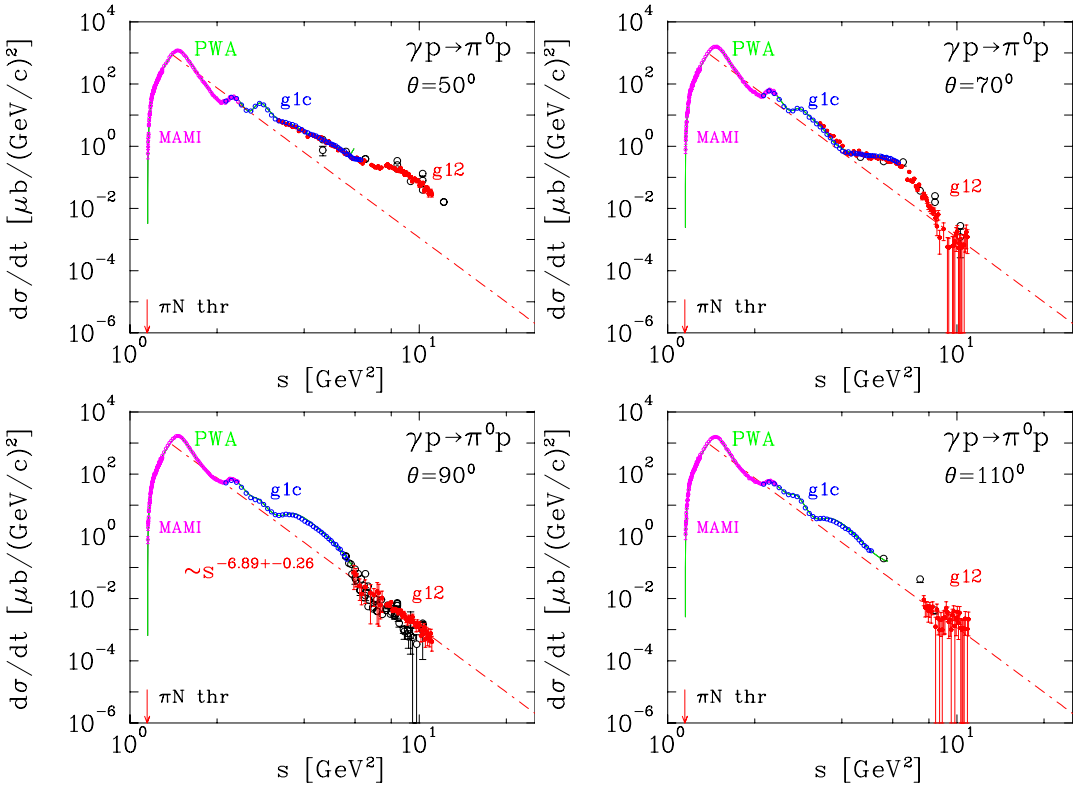

FIG. 1. The differential cross section for the $\gamma p \to \pi^0 p$ reaction at $\theta_{cm} = 50°, 70°, 90°, 110°$, as a function of the center of mass energy squared. The data are from Ref. [20], [21] and [22], open circles are data from old measurements [23]. The red points are preliminary results from a recent analysis of the CLAS g12 data. At high energies and large angles the results are consistent with the s^{-7} scaling expected from the quark counting rule. The dash dotted line is a result of the fit performed at $\theta = 90°$ with power function $\sim s^{-n}$ leading to $n = 6.89 \pm 0.26$.

may be due to different t ranges depending on the center of mass angle at fixed s as presented in Fig. 2. At lower angles t values are much smaller than s in the range of this data, therefore condition of counting rule [13], which requires large values of all three Mandelstam variables $s \sim t \sim u \gg \Lambda(QCD)$, is not fulfilled. The charged

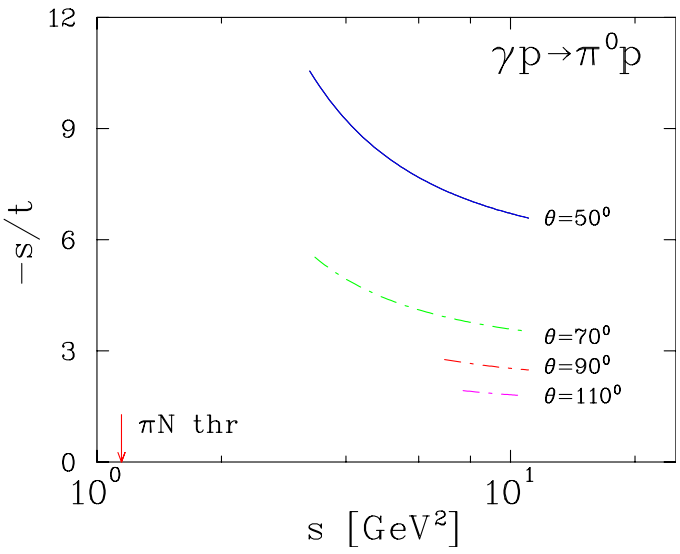

FIG. 2. s/t ratio for different center of mass angles as a function of invariant energy s.

pion photoproduction data at the highest energies also indicate a similar s^{-7} power law trend as is seen in Fig. 3.

The scaling behavior has been studied extensively in deuteron photo-disintegration experiments at SLAC and JLab [30] - [33]. Onset of the scaling behavior has been observed [32, 33] at a surprisingly low momentum transfer of 1.0 $(\mathrm{GeV/c})^2$ to the nucleon. Scaling behavior has also been observed in pion photoproduction, most recently in neutral pion production as shown in Fig. 1. However, polarization measurements on deuteron photo-disintegration [34] and in neutral pion photoproduction [35, 36], show disagreement with hadron helicity conservation in the same kinematic region where the quark counting behavior is apparently observed. These paradoxes make it essential to understand the exact mechanism governing the early onset of scaling behavior. Towards this goal, it is important to look closely at claims of agreement between the differential cross section data and the quark counting prediction and also to examine it over large angular range.

A large fraction of the pion photoproduction data at the highest energies have

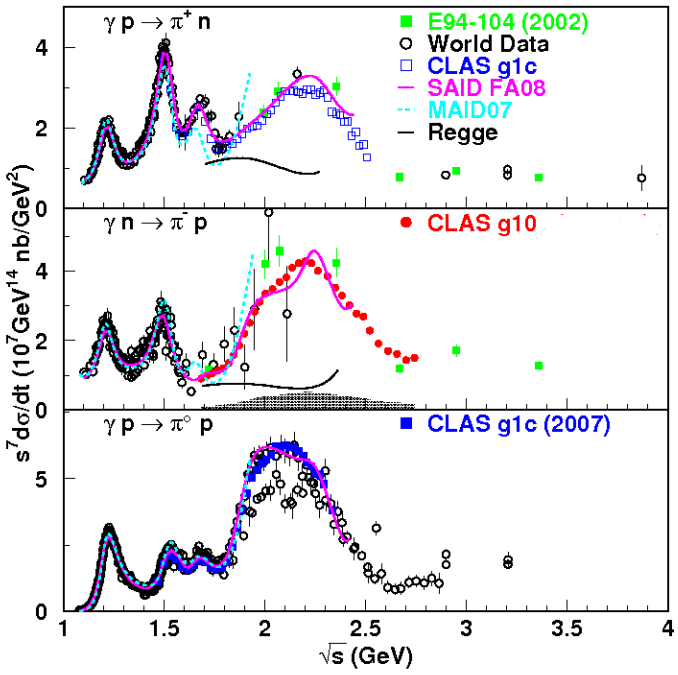

FIG. 3. The scaled differential cross section, $s^7 \frac{d\sigma}{dt}$ as a function of $\sqrt{s}$ at a center-of-mass angle of 90° for $\gamma p \to \pi^+ n$ channel (top panel), the $\gamma n \to \pi^- p$ channel (middle panel) and $\gamma p \to \pi^0 p$ (bottom panel). The data from JLab E94-104 are shown as green solid squares [24] and the CLAS π^+ data [21] are shown as magenta open squares, the π^- results [25] are shown as red solid circles and the π^0 results [21] are show as magenta solid squares. The SAID SP09 results [26] are shown as the blue solid curves in all three panels. The prediction from a Regge approach [27] is shown in the top and middle panels by black solid curves. The black open circles are the world data collected from Refs. [28, 29]

been collected using the "bremsstrahlung end point" technique. At the upgraded JLab, because of the fixed electron beam energy the end point technique would be restricted to very narrow range of energies and is thus no longer very effective. A high resolution, radiation-hard neutral particle detection facility will provide an

alternative method to measure wide angle π^0 photoproduction. The Neutral Particle Spectrometer under construction in Hall-C exactly fits the bill and will enable us to test the reaction mechanism of π^0 photoproduction. We propose to measure the differential cross-section $\frac{d\sigma}{dt}$ for the $p(\gamma, \pi^0)p$ processes over a range of center-of-mass angles in a photon energy between 5.0 and 10 GeV. We propose to use the data collected by the WACS experiment [11] at $E_{beam} = 8.8$ and 11.0 GeV to extract the π^0 cross section which is the largest source of physics background for the WACS experiment. In addition we propose to use the setup of the WACS experiment for additional measurements with 6.6 GeV electron beam at $70^\circ \leq \theta_{cm} \leq 105^\circ$ and one additional kinematics at 90° c.m. angles at $E_{beam} = 11$ GeV. Using the high luminosity and energy upgraded CEBAF, one can test the dominance of the handbag mechanism in pion photoproduction and also investigate its scaling behavior in detail to help identify the exact nature and the underlying mechanism responsible for scaling.

2. PHYSICS MOTIVATION

The main physics goals for measuring the π^0 cross section using the new NPS facility are to address the following questions:

1. Does the exclusive photopion production reaction proceed through the interaction of the photon with a single quark?

2. What is the energy scale for the transition from non-perturbative to pertubative mechanisms and/or soft to hard factorization mechanisms?

3. What can we learn about the non-perturbative structure of the proton using wide angle exclusive processes in general and pion photoproduction in particular?

We briefly discuss the current status of pion photoproduction models and the existing data and what is needed to be able to address the questions posed above.

2.1. The Handbag Mechanism and GPD-based Models

The introduction of the handbag mechanism has provided new possibilities for the interpretation of hard exclusive reactions. In this approach, the reaction is factorized into two parts, one quark from the incoming and one from the outgoing nucleon participate in the hard sub process, which is calculable using pQCD. While the soft part consists of all the other partons that are spectators and can be described in terms of GPDs [1]. This is illustrated in Fig. 4, where the hard exclusive meson (M) photo-production process factorizes into, $\gamma + q \rightarrow Mq$ and GPDs describing the soft hadronparton transitions. The handbag mechanism is applicable when the Mandelstam variables, s, t, u, are large as compared to a hadronic scale of order 1 GeV. The GPDs contain a wealth of information about the transverse distance and angular momentum of the quarks in the proton. They provide a unified description of nucleon structure, a common framework that can be applied to inclusive, semi-inclusive, and exclusive reactions. Presently, experimental access to

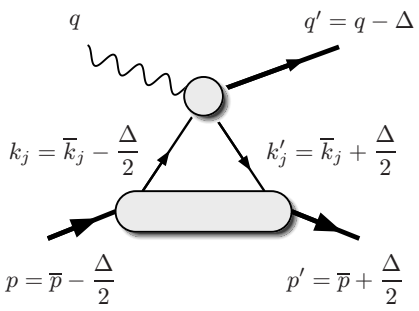

FIG. 4. The handbag diagram for photoproduction of mesons. The large blob represents a baryon GPD, while the small one stands for meson photoproduction off quarks.

such GPDs is amongst the highest priorities in intermediate energy nuclear/particle physics. However, access to the GPDs is intrinsically related to the soft-hard factorization. All order proofs of factorization exists only for deeply virtual processes. Factorization is particularly simple in the wide-angle processes, where it has been shown to hold to next-to-leading order in Compton scattering and to leading order in photoproduction of mesons. However, it is still uncertain at which Q^2 value one will reach the factorization regime, where leading-order perturbative QCD is fully applicable.

Recently, a new GPD based calculation by Diehl and Kroll [8] for wide angle Compton scattering, has been shown to agree well with experimental data.

The photoproduction of neutral pions at large c.m. angles is the next simplest reaction that can be tested against these GPD models. In ref. [4] the GPD based model of ref. [8] has been applied to predict angular dependence of scaled photoproduction cross section of π^0, presented in Fig. 5 (left panel). Preliminary experimental data from g12 CLAS run period [22] are presented on the right panel. The theoretical predictions are several orders of magnitude lower than experimental data.

One of the reasons for this failure may be due to one-gluon exchange mechanism for the generation of the meson and not the handbag mechanism itself. Although,

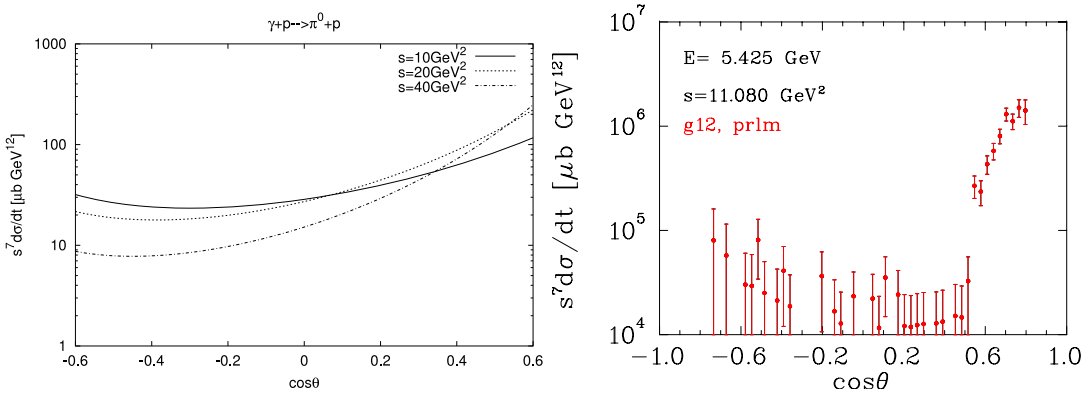

FIG. 5. Left panel is Fig.7 from [4]. Right panel- preliminary experimental data from CLAS [22]

.

the cross sections do not match experiments, H.W.Huang *et al.*, have also calculated other signatures of the handbag mechanism in wide-angle photoproduction of pseudo scalar mesons [9].

In their calculating of the $\pi^{\pm}$ cross sections ratio, the form factors cancel out and neglecting quark helicity flip contributions they obtain [9];

$$\frac{d\sigma(\gamma n \to \pi^- p)}{d\sigma(\gamma p \to \pi^+ n)} = \left(\frac{e_u s + e_d u}{e_u u + e_d s}\right)^2 . \tag{1}$$

This result coincides with the leading-twist prediction and are in surprisingly good agreement with experimental results from JLab [24] (see Fig. 6). It is surprising given the small photon beam energies involved.

Thus, there is an indirect indication from experiment that the handbag mechanism may be at work in these processes under the assumption of negligible quark helicity flip contributions.

The same formalism can be used to obtain the $\pi^0/\pi^{\pm}$ cross section ratios, however, in this case the form factors do not cancel out and a model of the form factors must be used to obtain the ratio. The predicted ratio for $\pi^0/\pi^{\pm}$ also disagree with data

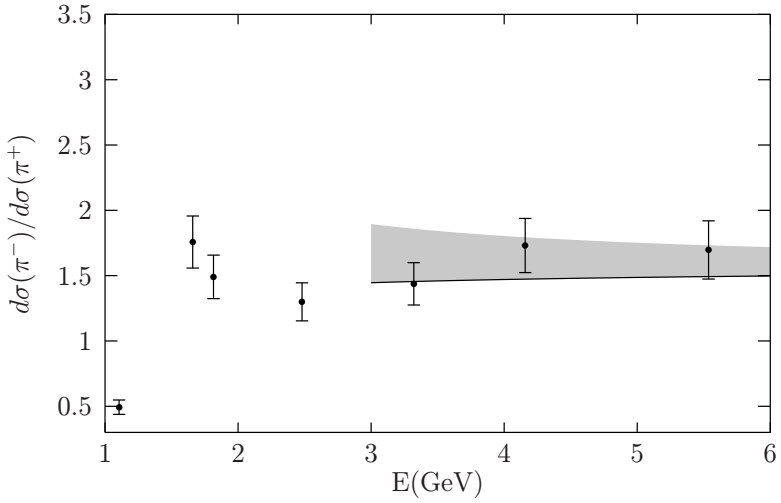

FIG. 6. The ratio of the $\gamma n \to \pi^- p$ and $\gamma p \to \pi^+ n$ cross sections versus photon beam energy E, at a c.m.s. scattering angle of 90°. Data are taken from [24]. The solid line is the handbag prediction, with the uncertainties due to target mass corrections is indicated by the shaded band.

by about an order of magnitude, just as the measured cross sections disagree with the calculations.

Several new calculations on wide-angle Compton scattering have recently become available [5], [6], [7], [8] and they can reproduce the measured cross sections. In case of π^0 photoproduction not only theory must be further developed, but also a new higher precision measurements of the π^0 cross sections in wide energy and angular range are needed to resolve the discrepancy and to motivate calculations of the π^0 cross section that would help verify the dominance of the handbag mechanism and/or help identify missing dynamical mechanisms of π^0 photoproduction.

2.2. Constituent Counting Rule

The constituent counting rule predicts the energy dependence of the differential cross section at fixed center-of-mass angles for an exclusive two-body reaction at high energy and large momentum transfer as follows:

$$d\sigma/dt = h(\theta_{cm})/s^{n-2}, \tag{2}$$

where s and t are the Mandelstam variables, s is the square of the total energy in the center-of-mass frame and t is the momentum transfer squared in the s channel. The quantity n is the total number of elementary fields in the initial and final states, while $h(\theta_{cm})$ depends on details of the dynamics of the process. In the case of pion photoproduction from a nucleon target, the quark counting rule predicts a s^{-7} scaling behavior for $\frac{d\sigma}{dt}$ at a fixed center-of-mass angle.

The quark counting rule was originally obtained based on dimensional analysis under the assumptions that the only scales in the system are momenta and that composite hadrons can be replaced by point-like constituents. Implicit in these assumptions is the approximation that the class of diagrams, which represent on-shell independent scattering of pairs of constituent quarks (Landshoff diagrams) [37], can be neglected. Also neglected were contributions from quark orbital angular momentum, which are power suppressed but can give rise to hadron helicity flipping amplitudes. These counting rules were also confirmed within the framework of perturbative QCD analysis up to a logarithmic factor of α_s and are believed to be valid at high energy, in the perturbative QCD region. Such analysis relies on the factorization of the exclusive process into a hard scattering amplitude and a soft quark amplitude inside the hadron. It has also been demonstrated that the counting rules for hard exclusive processes can arise from the correspondence between the anti-de Sitter space and conformal field theory [18] which connects superstring theory to

superconformal gauge theory.

Many exclusive reactions [12, 28] at high energy and large momentum transfer appear to obey the CCR. A similar trend, i.e. global scaling behavior, has been observed in deuteron photo-disintegration experiments [31–33] and in photoproduction of charged pions [24] at a surprisingly low transverse momentum value of ~ 1.1 (GeV/c)^2. The other natural consequence of pQCD: the helicity conservation selection rule, tends not to agree with data in the experimentally tested region. Hadron helicity conservation arises from quark helicity conservation at high energies and the vector gluon-quark coupling nature of QCD and by neglecting the higher orbital angular momentum states of quarks or gluons in hadrons. The same dimensional analysis which predicts the quark counting rule also predicts hadron helicity conservation for exclusive processes at high energy and large momentum transfers. If hadron helicity conservation holds, the induced polarization of the recoil proton in the unpolarized deuteron photo-disintegration process is expected to be zero. Polarization measurements in deuteron photo-disintegration[34] and π^0 photoproduction [35, 36] have been carried out at JLab. For deuteron photo-disintegration, while the induced polarization does seem to approach zero around a photon energy of 1.0 GeV at 90° center-of-mass angle, the polarization transfer data are inconsistent with hadron helicity conservation. The results from π^0 photoproduction are also inconsistent with hadron helicity conservation.

The entire subject is very controversial. Isgur and Llewellyn-Smith [16] argue that if the nucleon wave-function has significant strength at low transverse quark momenta ($k_\perp$), then the hard gluon exchange (essential to the perturbative approach) which redistributes the transferred momentum among the quarks, is no longer required. The applicability of perturbative techniques at these low momentum transfers is in serious question. There are no definitive answers to the question-*what is the energy threshold at which pQCD can be applied?* Indeed the exact mech-

anism governing the observed quark counting rule behavior remains a mystery.

2.3. New Developments

A number of developments have generated renewed interest in this topic. For example, Zhao and Close [38] have argued that a breakdown in the locality of quark-hadron duality (dubbed as "restricted locality" of quark-hadron duality) results in oscillations around the scaling curves predicted by the counting rule. They explain that the smooth behavior of the scaling laws arise due to destructive interference between various intermediate resonance states in exclusive processes at high energies, however at lower energies this cancellation due to destructive interference breaks down locally and gives rise to oscillations about the smooth behavior.

On the other hand, Ji *et al.* [17] have derived a generalized counting rule based on pQCD analysis, by systematically enumerating the Fock components of a hadronic light-cone wave function. Their generalized counting rule for hard exclusive processes include parton orbital angular momentum and hadron helicity flip, thus they provide the scaling behavior of the helicity flipping amplitudes. The interference between the different helicity flip and non-flip amplitudes offers a new mechanism to explain the oscillations in the scaling cross-sections and spin correlations. Brodsky *et al.* [19] have used the anti-de Sitter/Conformal Field Theory correspondence or string/gauge duality [18] to compute the hadronic light front wave functions exactly and it yields an equivalent generalized counting rule without the use of perturbative theory. In a further test of these approaches, calculations of the nucleon form factors including quark orbital angular momentum in pQCD [39] and those computed from light-front hadron dynamics [19] both seem to explain the $\frac{1}{Q^2}$ fall-off of the proton form factor ratio, $G_E(Q^2)/G_M(Q^2)$, measured at JLab in polarization transfer experiments [40].

As mentioned earlier, the π^0 photoproduction is one of the few exclusive processes

where the scaling behavior had not been verified and there is a lack of consistent data at high values of Mandelstam variables (s, t and u). Preliminary results from CLAS [22] seem to suggest the onset of scaling at 90° c.m. angle. Thus, to verify the scaling of the cross-section of neutron pion photoproduction process and to understand its origin, it is imperative that we do a scan of the scaling region for the $\gamma p \to \pi^0 p$ processes and extend measurements to much higher center-of-mass energies over a range of center-of-mass angles. Using the high resolution (position and energy) calorimeter under construction in Hall-C one can scan over larger energy and angular range and help verify the scaling behavior and study its origins.

2.4. Summary of motivations

The π^0 cross sections at wide angles and large momentum transfers will provide tests of the dominance of handbag mechanism. They will also help identify any missing dynamical mechanism in the handbag approach.

The π^0 cross sections will help study the details of the energy and angular dependence of the scaling and help understand the exact mechanism behind the relatively early onset of scaling. It will also help investigate the details of the agreement with scaling laws and provide insight into any oscillations about the scaling behavior.

All of these results will help identify the the energy scale for the transition from the soft to hard factorization regimes and help understand the non-pertubative structure of the proton.

3. THE PROPOSED MEASUREMENT

We propose to carry out a measurement of the photo-pion production cross-section for the $\gamma p \to \pi^0 p$ process on a liquid hydrogen target over a pion center-of-mass angle in the range $70^\circ < \theta_{cm} < 105^\circ$, and E_γ from $\sim$ 6 GeV to 10 GeV. The π^0

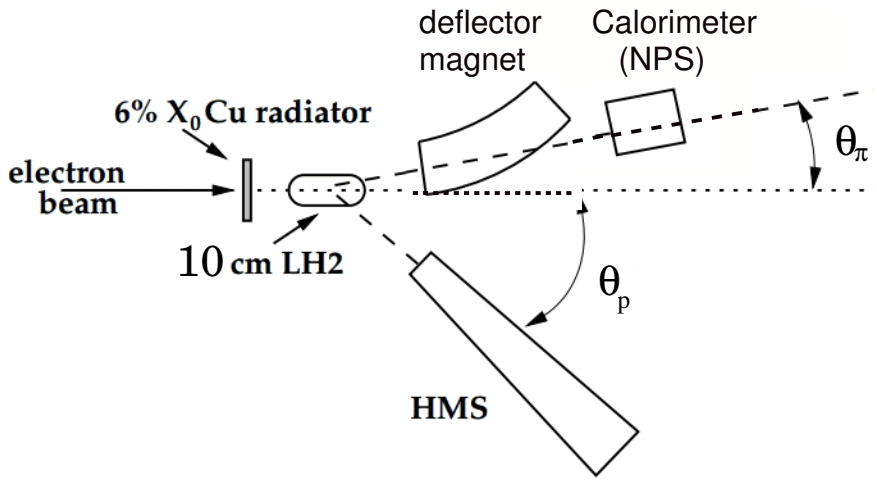

FIG. 7. Schematic of the experimental setup. This figure is reproduced from the WACS proposal with permission.

.

photoproduction is the dominant background for the WACS experiment. Thus we propose to use the same setup as the WACS experiment and extract the π^0 cross section from the same data which will be collected during the WACS experiment. The recoil protons will be detected in the High-Momentum Spectrometer (HMS) in standard configuration. Photons from π^0 decay will be detected by the Neutral Particle Spectrometer (see Fig. 7). Key elements of the proposed experiment are briefly described here with detailed descriptions given in the WACS proposal [11].

3.1. The CEBAF Electron Beam

The maximum electron beam energy required is 11 GeV, in addition beam energies of 8.8 GeV and 6.6 GeV are also required. Beam with currents up to 60 μA will be incident on a 10 cm long liquid hydrogen target, resulting in an average luminosity

of $\mathcal{L}_{ep} = 1.6\ \times 10^{38}/cm^2/s$.

3.2. Target and Radiator

The experiment will utilize one of the standard Hall C liquid hydrogen (LH2) targets with a 10 cm-long machined cell with aluminum walls of 5 mil thickness, which has been successfully employed in many experiments at JLab. The copper radiator with a thickness of $t_{rad}/X_0 = 0.06$ (6% of radiation length) will be mounted on the cell block about 25 cm upstream of the cell entrance window. The distance between the target and the radiator and the high photon energies help avoid the background produced on the walls of the target and keeps the photon beam spot compact, which allows both accurate measurement of the proton momentum with the vertical bend spectrometer and operation with high luminosities. Further, the distance between the radiator and the target allows additional shielding to be installed to reduce scatterings from the radiator. Note that in the rate simulations described later in the proposal, the effective thickness of the radiator was assumed to be slightly larger, $t_{rad}/X_0 = 0.08$, due to additional radiative processes in the target and the virtual photon flux. This description is reproduced from the WACS proposal.

3.3. Deflection Magnet

Previous RCS experiments have shown that a deflection magnet provides an effective way to discriminate between elastic electron and photon scattering events. When a deflection magnet is used there is no need for a veto detector, which in turn allows for at least a ten times higher photon/electron beam intensity. The deflection magnet for the new WACS experiment has been designed with a large enough aperture to cover the entire calorimeter and provide adequate electron deflection while

minimizing the magnetic field on the beam line. The description of the magnet and its optimization procedure has been reproduced from the WACS proposal.

One of the key aspects in discriminating the signal from background, in both the WACS and photopion experiments, is a reliable comparison of the expected and measured electron-proton (calorimeter-HMS) correlation. The angular spread of this correlation is smaller in the out-of-plane direction because it is defined only by angular resolution; in contrast, it is larger in-plane because its dominant contribution comes from the proton momentum reconstruction resolution for a given proton momentum. Typically the out-of-plane resolution relevant for the e-p correlation is twice as good as the in-plane resolution. The bending direction for elastic electrons should therefore be vertical (magnetic field horizontal) in order to minimize the required deflection of electrons and the resulting value of the field in the deflection magnet.

Additional information about the magnet design is presented in Ref. [11].

In order to extract the π^0 cross section the distribution of the pion related events need to be well understood. The deflector magnet must therefore relocate the electrons sufficiently far from the π^0 decay events. This can be accomplished by a sufficiently strong deflector magnet. A magnet that will be able to provide a field integral of up to $\int B \cdot dl \sim 0.6Tm$ has been designed and will be constructed for the proposed WACS experiment. It will be placed as shown in Fig. 7 and an image of the magnet is shown in Fig. 8. We will use the same magnet for the additional kinematics covered in this proposal.

3.4. The High Momentum Spectrometer

The recoil protons in the proposed experiment will be detected by the High-Momentum Spectrometer (HMS), which is part of the standard equipment of Hall

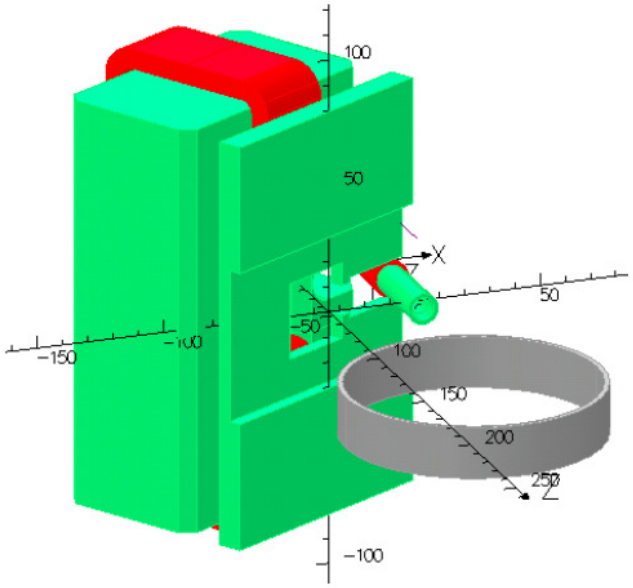

FIG. 8. An image of the deflection magnet for the WACS experiment from the TOSCA analysis package, with the magnet placed at a 30 degree scattering angle with 110 cm between the magnet center and the target. This image is reproduced from the WACS proposal.

C. The HMS is a high resolution ($\delta p/p < 10^{-3}$) magnetic spectrometer in a QQQD magnet configuration with a maximum momentum of 7.5 GeV/c and a momentum acceptance of 18 %. It has an octagonal input aperture with an effective solid angle coverage of approximately 6 msr and can be positioned to angles greater than 12.5°. The detector package of the HMS consists of two vertical drift chambers for track reconstruction, scintillator hodoscopes for timing, as well as a gas C̈erenkov counter, an aerogel C̈erenkov counter, and a segmented lead-glass shower calorimeter for particle identification. If needed, the shower calorimeter could be used in the trigger. The HMS can be tuned in parallel-to-point mode (for optimal in-plane angle accuracy) or point-to-point mode (for best vertex reconstruction). In the proposed experiment it will be used in the latter mode in which extended targets can be

accommodated with a vertex reconstruction accuracy of 1 mm, and where both in-plane and out-of-plane angular resolutions are about 0.8 mrad. In this proposal the SIMC simulation package was used for determination of the actual momentum and angular resolutions, which included scattering in the target material as well as reconstruction effects. The simulation is further elaborated in a later section. This description is reproduced from the WACS proposal.

3.4.1. Expected Rates

The DINREG Monte Carlo code developed by the RadCon group at JLab [41] has been used to calculate the expected proton and π^+ rates in the HMS for each of the proposed kinematic settings. Fig. 9 shows the simulated HMS singles rates, and the simulated proton-to-π^+ ratio. The maximum HMS singles rate of 75 kHz is at kinematic point 3F, which corresponds to a beam current of 15μA. The equivalent trigger rate (for protons only) for this same kinematic point is 7.5 kHz. These rates are well within the capabilities of the HMS.

3.5. The Photon Calorimeter

The photon calorimeter for this experiment will be the new Neutral Particle Spectrometer [10] being constructed in Hall-C. This photon calorimeter will consist of a rectangular array of 29 (horz) $\times$ 35 (vert) $PbWO_4$ crystal blocks with dimensions 2.05$\times$2.05 $\times$ 18 cm^3. Each crystal is attached to a photo-multiplier tube and base. The proposed calorimeter is based on the existing HYCAL calorimeter [42]. Fig. 10 shows an array of crystal blocks that will closely resemble the one which will be used in the proposed experiment.

The PMTs are shielded from ambient light in a light-tight box that contains an air cooling system, whose main purpose is to prevent the PMTs from overheating

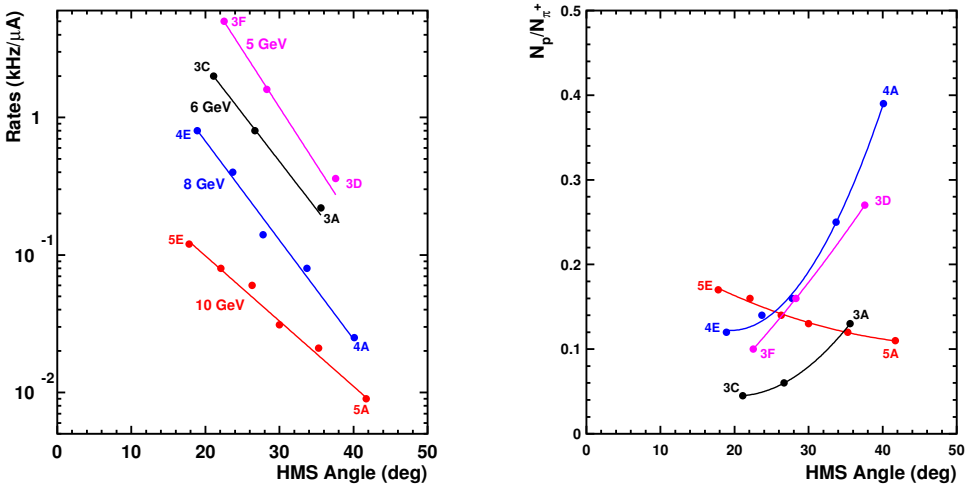

FIG. 9. Simulated raw singles rates in the HMS (left) and proton-to-π^+ ratio (right).

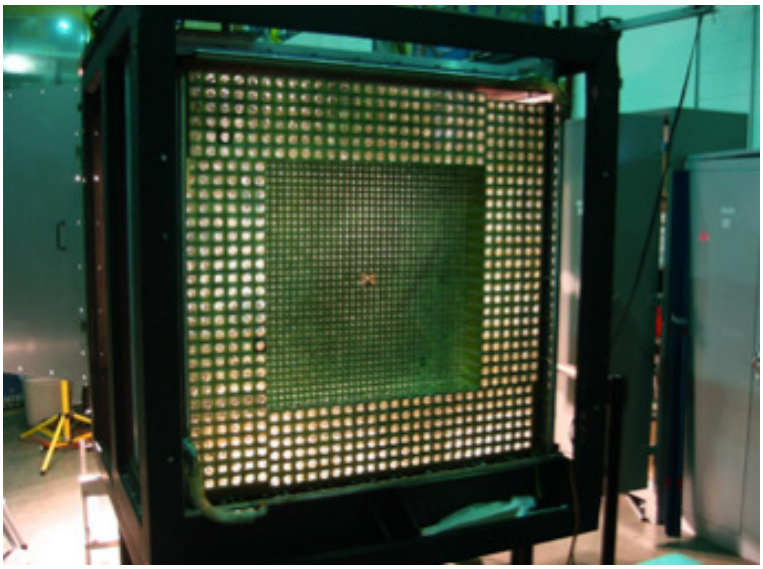

FIG. 10. The central high-resolution $PbWO_4$ part of the HYCAL detector will be used in the NPS.

and aid in the overall stable operation of the calorimeter. The yield of the $PbWO_4$ crystals is temperature dependent, with $\approx 2\%/^{\circ}C$ deterioration of light yield around

room temperature. HV and signal-cable systems are also contained in the light box encasing the PMTs. The calorimeter will be equipped with a system that distributes light pulses to each calorimeter module. The main purpose of this system is to provide a quick way to check the detector operation and to calibrate the dependence of the signal amplitudes on the applied HV. The detector response to photons of a given energy may drift with time, due to drifts in the PMT gains and to changes in the glass transparency caused by radiation damage. For this reason, the gain monitoring system will also allow measurements of the relative gains of all detector channels during the experiment. The calorimeter can be moved into the hall without being disconnected from the frontend electronics, which is located in racks a few feet behind the main detector components. The position of the photon arm will be adjusted for each kinematic setting to match the angular position of the HMS. The calorimeter will most likely be placed on rails and repositioned by sliding along these rails. To shield from radiation it will be very beneficial to place a 10 cm thick plastic cover with an effective surface area thickness of approximately $10 g/cm^2$ in front of the calorimeter. This description is reproduced from the WACS proposal.

3.5.1. Expected Rates

DINREG Monte Carlo simulations for the expected NPS singles rates have also been performed for each of the proposed kinematic points [41]. The total number of γ, e^+ and e^- incident on the calorimeter with energy greater than 1 GeV gives a maximum singles rate of 1.2 MHz. The simulated rates are shown in Fig. 11.

3.6. Trigger and DAQ

The HMS trigger will be the only trigger for this experiment. This is possible because of the modest event rate expected in the proton arm at high photon beam

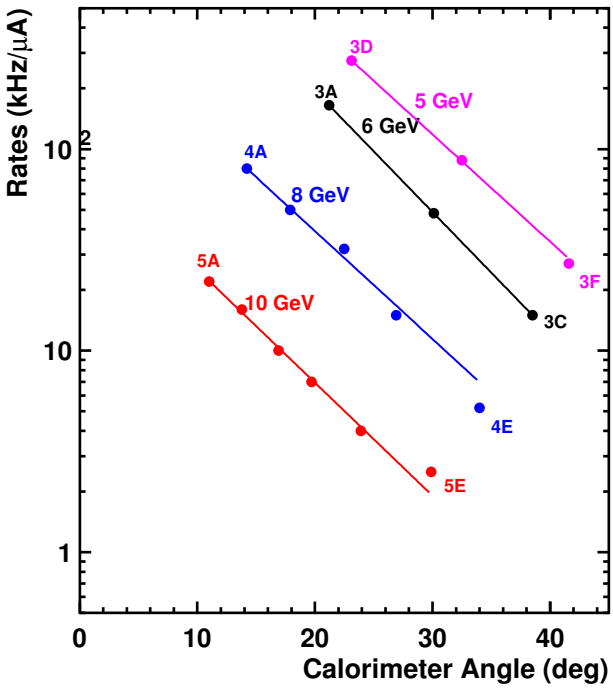

FIG. 11. Simulated raw singles rates in the NPS

.

energies and because the new HMS and NPS pipeline based electronics will be dead-time free. Hence each particle detected by the HMS will trigger the DAQ readout of both the HMS and the calorimeter. The cluster summing trigger for the calorimeter will not be implemented. The read-out of the NPS FADCs will be controlled by FPGA based hardware, which will be programmed to recognize where a hit has occurred and will read out only the relevant group of FADC modules. This will avoid generation of extraneous data.

The typical NPS event size is expected to be 1 kB, while the HMS event size is expected to be less than 2 kB [11]. Since the trigger will be formed by the HMS, the maximum data throughput will be at kinematic point 4E, where the expected

trigger rate is 7 kHz. These numbers, along with the expected NPS singles rates gives a maximum DAQ rate of ~ 2 MB/s and a total data set of around 1 TB. Both these numbers are well within the capabilities of the online DAQ and data storage facilities. This description is reproduced from the WACS proposal.

3.7. Radiation Budget

The high luminosity required in the proposed experiment could result in loss of the energy and coordinate resolutions of the calorimeter due to pileup. Long operation at high radiation load could cause radiation damage to the crystals and deterioration of their performance.

In order to estimate the potential for radiation damage to the calorimeter crystals, the DINREG simulation code was used. The total dose rate incident upon the NPS calorimeter for each kinematic point and the proposed running conditions has been calculated, with the results shown in Fig. 12. The maximum expected rate is 840 rad/h for kinematic point 4D. Assuming the dose is deposited over the full crystal length, this simulation gives a total accumulated dose estimate for the full beam-time of 153 kRad. This does not include the effects of shielding the calorimeter from low energy electromagnetic radiation, with shielding the radiation dose is expected to be 45 krad. Although these numbers are significant, they are still acceptable according to a study [44], which found that at a value of 1 Mrad, the light output reduction for $PbWO_4$ is around 2%.

Using the data from the previous RCS experiment in 2002, the radiation level in Hall C during the proposed experiment is expected to be of the order of 200 mR/hour. The radiation load could be reduced by a factor of 2, if necessary, by using modest local shielding of the radiator and the target installed at angles above 50°. This description is reproduced from the WACS proposal.

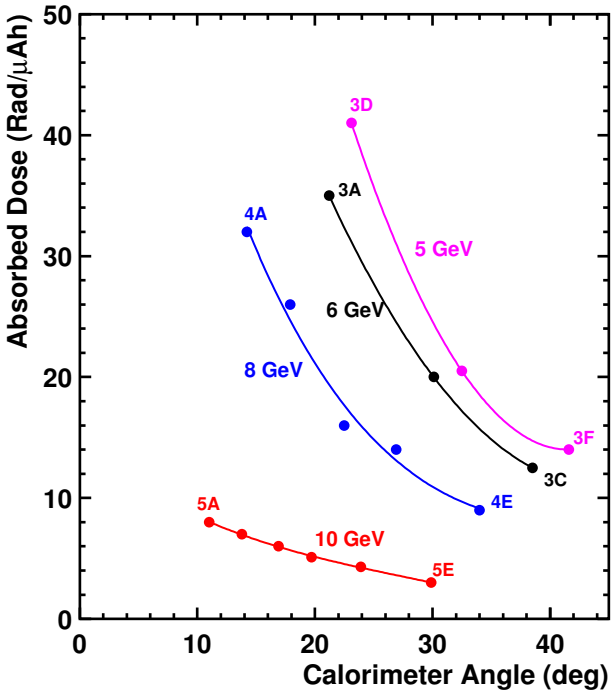

FIG. 12. Simulated radiation dose in the NPS.

.

3.8. Energy and Coordinate Resolution

The energy of the particle detected in the calorimeter is calculated from a sum of the signals in several crystals (up to 9) which form a cluster. The noise in the ADC used for a measurement of the signal from an individual crystal contributes to the detector energy resolution. In a high-rate experiment the ADC noise increases, which can be characterized by the ADC pedestal width. Using the observed 5-6 MeV pedestal width observed in the previous RCS experiment, the expected pedestal width for this proposal is projected to be around 50 MeV. The effect of the background on the energy resolution could be estimated from this estimated

pedestal width and the number of modules in the cluster. It is expected to be on the level of 110-150 MeV or 3.3-4.5%, a similar estimate shows that the effect on the coordinate resolution is around 0.5 mm. This description is reproduced from the WACS proposal.

3.9. Kinematic settings

The differential cross section for Wide-angle π^0 photoproduction will be determined at photon energies of 5.0 - 10.0 GeV at $70^\circ < \theta_{cm} < 105^\circ$. The kinematics for the two standard beam energies of 8.8 GeV and 11 GeV are exactly identical to those for the newly proposed WACS experiment. However, unlike the WACS experiment the π^0 experiment will measure the cross section at one additional kinematic setting at 11.0 GeV beam energy and 6 additional kinematic settings at a beam energy of 6.6 GeV. Kinematics for only the additional settings at 11.0 GeV and 6.6 GeV beams are shown in Table I, the kinematics settings at 8.8 and 11 GeV that are identical to the WACS experiment are not shown here. The coverage in $|t|$ and s for full experiment is shown in Fig. 13. In all cases, the scattering angles and momenta fall well within the allowed range for the HMS and the NPS and pose no practical difficulties in terms of positioning of the detector systems.

3.10. Monte Carlo Simulation

The WACS collaboration has developed a Monte Carlo simulation in order to study the feasibility of extracting the RCS signal from large backgrounds due to the π^0 decay and elastic e-p scattering. Events are first generated over a much broader kinematic range compared to the detector acceptances, according to cross section parameterizations of the three reaction types: RCS, neutral pion photoproduction, and elastic *ep* scattering. We have used this same Monte Carlo simulation for our

TABLE I. Table of kinematics for the $p(\gamma, \pi^0 p)$ reaction at $\mathrm{E_{beam}}$ of 11.0 at pion c.m. angle of 90° and 6.6 GeV at pion c.m. angle of 70, 90 and 105°. These settings are in addition to the setting used in the WACS proposal.

	E_γ	θ^π_{cm}	$\sqrt{s}$	$\lvert t\rvert$	θ_p (lab)	θ_{π^0} (lab)	P_p	P_{π^0}
3A	6.0	70	3.48	3.44	35.6	21.2	2.602	4.170
3B	6.0	90	3.48	5.21	26.7	30.1	3.595	3.218
3C	6.0	105	3.48	6.98	21.1	38.5	4.334	2.50
3D	5.0	70	3.20	3.14	37.6	23.1	2.251	3.497
3E	5.0	90	3.20	4.81	28.3	32.5	3.079	2.716
3F	5.0	105	3.20	5.32	22.5	41.6	3.691	2.125
5F	10.0	90	4.43	8.01	22.1	23.9	5.632	5.227

studies. In order to study the feasibility of extracting the photoproduced π^0, we have added two more reactions 2-pion production and η production. The parameterizations of the cross sections are based on E99-114 data in the case of RCS and neutral pion photoproduction [45] and the Bosted fit to the Sachs form factors for elastic *ep* scattering events [46]. The 2-pion and η production cross sections were obtained from the Durham database [47]. The proton interactions in the target and HMS are then simulated using the standard Hall C SIMC simulation package, while the particles scattered towards the NPS (photons, pions and electrons) are simulated using dedicated software developed within the CERN Geant4 framework. This latter tool includes a realistic simulation of the target, scattering chamber, deflection magnet and the NPS. The technique developed and refined for identifying RCS events and extracting the associated yield, namely, one assumes two-body kinematics and uses the measured recoil proton variables to reconstruct a predicted hit position for the corresponding scattered photon at the NPS. The differences between the predicted

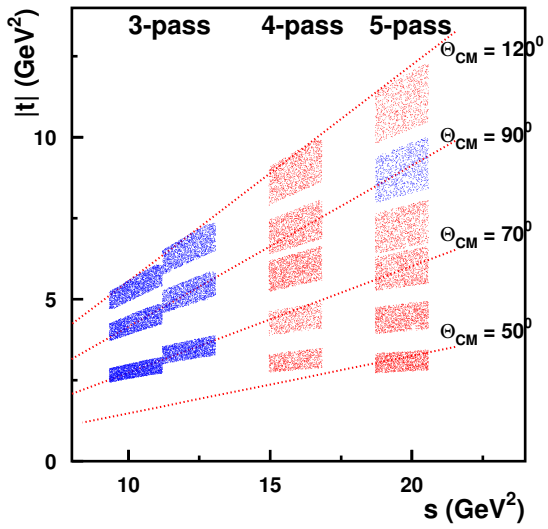

FIG. 13. Kinematic coverage with the 3 pass, 4 pass and 5 pass beams, determined by the HMS acceptance and a photon energy range of 1 GeV about the central setting. The WACS settings are shown in red while the π^0 only settings are shown in blue.

.

and measured NPS hit positions, δx and δy, are then used to identify the reaction from which a particular event originated. The distributions shown in Figs. 14 (obtained from the WACS collaboration) correspond to the difference between the expected NPS hit positions for a good proton track in the HMS and the center-of-gravity positions of the highest energy NPS cluster. One can see that the elastic ep events are centered at positive δy due to deflection in the magnet, RCS events are centered around zero, and events from detection of one of the photons from the decay of a neutral pion form a relatively broad background.

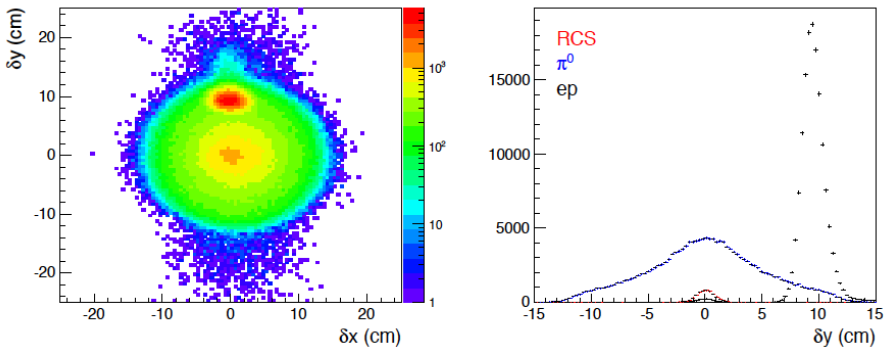

FIG. 14. Typical NPS hit difference distributions for kinematic point 4D. (Left)δx vs δy for all events. (Right) A projection on to δy for events in the central δx region. Figure obtained from WACS collaboration.

.

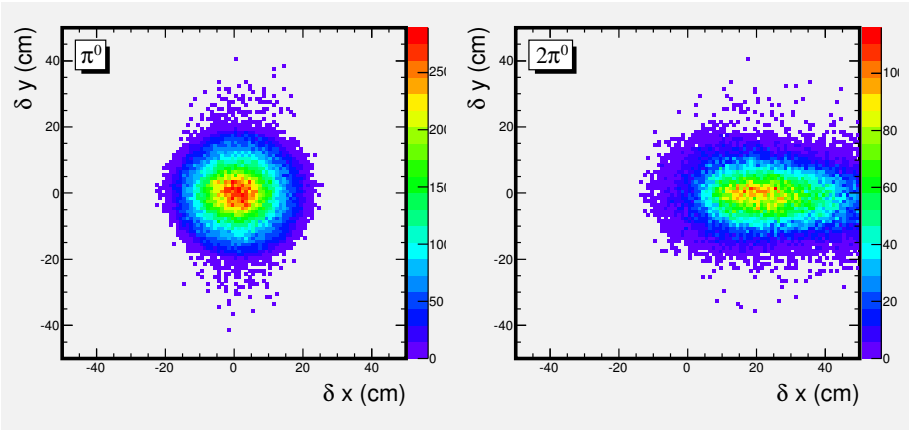

FIG. 15. (Left) δx vs δy for π^0 events for kinematic point 3B. (Right) δx vs δy for 2-π^0 events.

The same technique was found to work very well in distinguishing 1-pion from 2-pion events. In Fig. 15 we compare the δx and δy for single pion (left) and two pion (right) events. The photons from the decay of 2-pion events have relatively large δx, and once a cut corresponding to $\pm 1.5\sigma_x$ (where σ_x is the x-resolution of

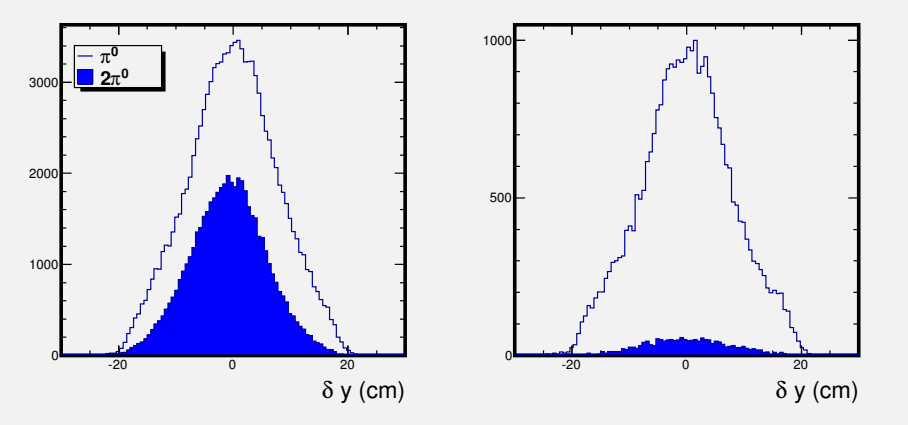

FIG. 16. Left:A projection on to δy for all π^0 and 2-π^0 events (shaded). Right: A projection on to δy for π^0 and 2-π^0 events (shaded) in the central δx region.

the calorimeter) is applied, very few of the 2-pion events end up being wrongly identified as 1-pion events, as seen in Fig. 16. These figures are for the situation with the worst $2-\pi/\pi$ ratio (kinematics 3F), and demonstrate that the technique is very effective in rejecting $2-\pi$ events. A more typical situation corresponding to kinematics 5B is shown in Fig. 17

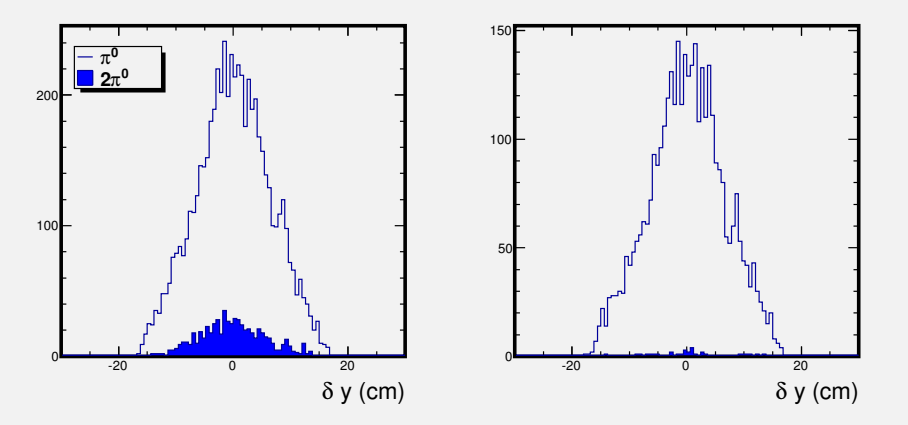

FIG. 17. Left:A projection on to δy for all π^0 and 2-π^0 events (shaded). Right: A projection on to δy for π^0 and 2-π^0 events (shaded) in the central δx region.

Above the η production threshold, the η events are indistinguishable from the 1-pion events, however the η production rates were negligible compared to the 1-pion rates. Fig. 18 shows all the η events detected (left) for the kinematics with the worst η/π^0 ratio (5D) and the events which survive the cut corresponding to $\pm 1.5\sigma_x$ (right), which are $< 1\%$ of the π^0 events.

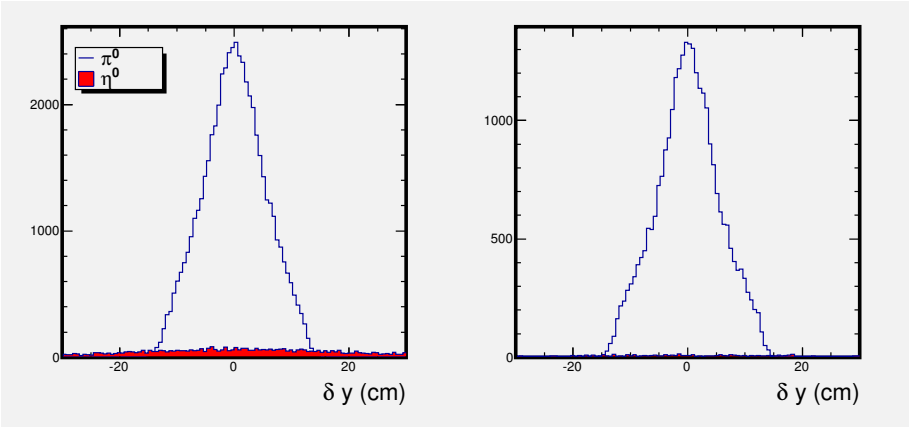

FIG. 18. Left:A projection on to δy for all π^0 and η events (shaded). Right: A projection on to δy for π^0 and η events (shaded) in the central δx region.

The free parameters associated with the experimental set-up i.e. the deflection magnet distance and field integral, as well as the NPS distance have been optimized with the Monte Carlo simulation for all kinematic settings in order to maximize the deflection of the electrons from *ep* events, minimize the resolution of the NPS hit difference distributions as well as the relative number of background events compared to the signal. The optimized values of the parameters of the experimental settings for the 6.6 GeV settings are shown in Table III. The parameters for the 8.8 and 11 GeV settings are identical to those in the WACS proposal [11] and are not repeated here.

Another interesting feature of this experiment will involve the dual role for the events close to the end point of the Bremsstrahlung spectrum which is well below

the two pion threshold. For these π^0 events there are no 2-pion or η backgrounds. Therefore, these events can also be used to optimize and then monitor the π^0 acceptance and efficiency of the calorimeter. The measured π^0 acceptance function can then be used to build better simulations of the calorimeter.

3.10.1. Physics Background

Although the deflection magnet deflects the *ep* elastic events away from the RCS peak it does not deflect it completely outside the NPS acceptance. Thus the *ep* events are the dominant background for the extraction of the π^0 yield. The ratio N_{ep}/N_{π^0} varies between 0.02 - 4.87, while the N_{RCS}/N_{π^0} varies between 0.07 - 2.17. Experience from previous JLab WCS experiments has shown that good calorimeter energy resolution, two-cluster analysis along with a Monte Carlo simulation can be used to fit the pion, the RCS and the *ep* events and extract the pion yield. For this reason, one other critical factor in the final values chosen for the NPS distance has been to ensure that the distribution of pion events in δx and δy is not artificially truncated by the NPS acceptance. The feasibility of separating the π^0 events from the RCS events is shown for each kinematic setting in the WACS proposal [11] and is not reproduced here. However, unlike the WACS experiment, 2π and η events are additional physics backgrounds in extracting the π^0 cross section. The ratio $N_{2\pi^0}/N_{\pi^0}$ varies between 0.012 - 0.053 and the N_{η}/N_{π^0} varies between 0.001 - 0.012, in the $1.5\sigma_x$ central δx - δy region. These cannot be the distinguished from the single pion events and will lead to an additional systematic uncertainty compared to the WACS experiment. Contribution from these events will be corrected by using an estimate from a Monte Carlo simulation.

3.10.2. Detector Resolution

Based on the experience from previous JLab WACS experiments, it has been established that the two-arm resolution for the calorimeter hit difference distributions, is dominated by i) proton multiple scattering and reconstruction in the proton spectrometer, and ii) the out-of-plane (δy) resolution is much better than the in-plane (δx) resolution, as a result of the fact that the latter includes significant contributions from the proton momentum and vertex resolutions. This is the primary reason that a horizontal magnetic field, and therefore vertical deflection, is critical to the success of the proposed measurements. Typical values for the expected NPS position and energy resolutions have been included in the Monte Carlo simulation, as have photon/electron interactions in the target, scattering chamber and a 10-cm plastic shield directly in front of the NPS which acts as a shield from low energy electromagnetic background. These result in a contribution to the resolution over all kinematic settings of around 0.35 cm. For the range of proton momenta considered in the present proposal (1.791 - 7.586 GeV/c), the in-plane angular resolution varies between 1.5 and 2.5 mrad, the out-of-plane resolution between 1.7 and 3.8 mrad, and the $\delta p/p$ resolution between 5 and 7.5×10^{-4}. It is primarily the last (although there is a small contribution from the vertex resolution) that leads to the δx resolution being poorer than the δy resolution. The NPS distance clearly plays a crucial role in determining the final values for the two-arm resolutions. It has therefore been optimized for all kinematic settings such that the out-of-plane resolution remains around or less than 1 cm at the two highest beam energies and less than 2 cm for the setting using the 6.6 GeV beam. The table of parameters for the experimental setup is shown in Tables II and III. The $\mathrm{E_{beam}}$ = 8.8 and 11 GeV are identical to the WACS experiment [11]. This description is reproduced from the WACS proposal.

TABLE II. Table of parameters for the experimental setup for the E_{beam} = 8.8 and 11 GeV settings where the π^0 cross section will be extracted. These are reproduced from the WACS proposal, except for the additional setting 5F to cover the 90° c.m. angle at the highest photon energy.

Label	D_{NPS}	D_{mag}	B	σ_x	σ_y	e-defl	$N_{ep\gamma}/N_{\pi^0}$	$N_{\pi^0\pi^0}/N_{\pi^0}$	N_{η}/N_{π^0}	N_{RCS}/N_{π^0}
	(m)	(m)	(T)	(cm)	(cm)	(cm)				
4B	7.0	1.65	1.00	2.21	0.75	10.74	1.12	0.022	0.006	0.90
4C	5.0	1.65	1.25	1.61	0.71	9.55	0.29	0.018	0.004	0.37
4D	3.5	1.10	1.50	1.36	0.79	9.24	0.11	0.021	0.004	0.21
4E	3.0	1.10	1.50	1.21	0.86	8.72	0.03	0.022	0.006	0.1
5B	9.0	2.45	0.875	2.63	0.71	8.71	4.18	0.012	0.012	1.39
5C	7.0	1.65	1.00	2.30	0.77	9.75	0.97	0.012	0.004	0.56
5D	6.0	1.65	1.25	2.18	0.79	9.91	0.69	0.012	0.008	0.36
5E	3.25	1.10	1.50	1.26	0.92	8.07	0.03	0.017	0.006	0.08
5F	5.0	1.10	1.50	2.16	0.82	9.57	0.43	0.015	0.006	0.22

3.11. Rates and Systematic Uncertainties

The expected RCS event rate for the kinematic settings given in Tables 2 has been calculated with the Monte Carlo simulation and yield extraction analysis technique described above. The event rate is the product of the luminosity, the cross section, and the acceptances of the detectors, as well as all other factors such as DAQ dead time, efficiency of the trigger, and the detectors and efficiency of the reconstruction analysis. The rate was calculated as:

$$N_{\pi^0} = \frac{d\sigma}{dt}\frac{(E_\gamma^f)^2}{\pi}\Delta\Omega_\gamma f_{\gamma p}\left(\frac{\Delta E_\gamma^f}{E_\gamma^f}\frac{t_{rad}}{X_0}\right)\mathcal{L}_{ep},$$

TABLE III. Table of parameters for the experimental setup for the E_{beam} of 6.6 GeV settings. These are in addition to the settings of the WACS experiment.

Label	D_{NPS}	D_{mag}	B	σ_x	σ_y	e-defl	$N_{ep\gamma}/N_{\pi^0}$	$N_{\pi^0\pi^0}/N_{\pi^0}$	N_{η}/N_{π^0}	N_{RCS}/N_{π^0}
	(m)	(m)	(T)	(cm)	(cm)	(cm)				
3A	5.0	1.1	1.25	2.27	0.89	12.8	0.25	0.020	0.002	0.41
3B	3.5	1.1	1.5	1.51	0.87	11.3	0.05	0.033	0.001	0.15
3C	3.0	1.1	1.5	1.40	0.82	10.2	0.026	0.039	0.001	0.076
3D	5.0	1.1	1.25	2.46	0.97	14.9	0.31	0.04	0.001	0.57
3E	3.5	1.1	1.5	1.55	0.96	12.9	0.052	0.052	0.001	0.19
3F	3.0	1.1	1.5	1.51	1.12	11.64	0.02	0.053	0.001	0.07

where $\frac{d\sigma}{dt}$ is the photopion cross section, the factor $\frac{(E_\gamma^f)^2}{\pi}\Delta\Omega_\gamma$ is the range of Δt for a given kinematics, $f_{\gamma p}$ is the fraction of events detected for a given range of photon energies E_γ^f, $\frac{\Delta E_\gamma^f}{E_\gamma^f}\frac{t_{rad}}{X_0}$ is the photon flux, i.e. the number of photons produced per incident electron (including photons produced in the target and virtual photons), and $\mathcal{L}_{ep}$ is the electron-proton luminosity.

The statistical precision that can be achieved, including the uncertainty due to the fluctuations in the $ep\gamma$ and RCS background is given by:

$$\delta_{stat} = \frac{\delta_{N_{\pi^0}}}{N_{\pi^0}} = \frac{\sqrt{(N_{\pi^0} + R_{ep\gamma}N_{\pi^0} + R_{RCS}N_{\pi^0})}}{N_{\pi^0}}$$

The raw singles rates in the HMS and NPS have been determined for events arising from RCS, elastic ep scattering and π^0 photoproduction. The HMS singles rates for π^+ photoproduction have also been calculated. These are shown for a corresponding electron beam current chosen for each kinematic setting in Tables IV and V. For all settings the HMS trigger rate will be well within the acceptable HMS operating parameters as determined in previous HMS experiments. The π^+ rates are such that

rejection of these events off-line via the kinematic reconstruction technique described in previous sections will be sufficient, without the need for any additional particle identification. This description is reproduced from the WACS proposal.

TABLE IV. Table of rates for the E_{beam} = 8.8 and 11 GeV settings. These are exactly the same as the settings for the WACS experiment except for setting 5F which is new. The beam time includes 7 hours for runs with radiator removed and for spectrometer moves. For setting 5F the overhead is only 3 hrs which includes 1 hr for runs without the radiator and 2 hrs for spectrometer move.

Setting	I_{beam}	$\dot{N}_{\pi^0}$	N_{π^0}	δ_{stat}	t
	(μA)	($\mu A^{-1} hr^{-1}$)		%	(hr)
4A	5	6.9	700	11	20+7
4B	15	6.7	2000	4	20+7
4C	30	8.1	4900	1.8	20+7
4D	60	6.9	12400	1.0	30+7
4E	60	7.1	17000	0.8	40+7
5A	15	2.7	800	15.7	20+7
5B	30	2.2	1600	6.4	25+7
5C	60	2.9	3400	2.7	20+7
5D	60	2.8	6600	1.8	40+7
5E	60	3.8	27000	0.6	120+7
5F	60	3.2	1000	4.1	5+3
Total					433

The three main sources of systematic uncertainties in the proposed measurement of the π^0 cross section are those associated with the yield extraction, the determination of the detector acceptance and efficiencies, and the determination of the total

TABLE V. Table of rates for the E_{beam} of 6.6 GeV settings. The beam time includes 1 hr for runs with radiator removed and 2 hrs for spectrometer moves.

Setting	I_{beam}	$\dot{N}_{\pi^0}$	N_{π^0}	δ_{stat}	t
	(μA)	($\mu A^{-1} hr^{-1}$)		%	(hr)
3A	15	31.1	2300	2.7	5+3
3B	15	45.4	3400	1.6	5+3
3C	30	48.2	7200	1.2	5+3
3D	15	45.1	3400	2.4	5+3
3E	15	59.4	4400	1.7	5+3
3F	15	59.5	4400	1.6	5+3
Total					48

photon beam flux. The extensive experience gained during the E99-114 and E07-002 experiments in combination with the Monte Carlo simulation studies detailed in the previous section is relied upon to make estimates of these various sources of systematic uncertainties. Adding the various contributions described below in quadrature, it is estimated that the total systematic uncertainty for the proposed measurement will be around 8% for the least favorable kinematic setting. Beginning with the total photon beam flux, there are contributions to this particular uncertainty from measurement of the accumulated electron beam charge, target thickness, and determination of the bremsstrahlung photon flux for a given energy range. This last dominates, while the others are estimated to be less than 1%. The utilization of redundant calculations of the bremsstrahlung flux (using both Geant4 and dedicated thick-target bremsstrahlung tools) and measurements using the actual data lead to confidence that this uncertainty can be kept around the 3% level. Furthermore,

previous experience working with the HMS, the simple geometry of the NPS, and the fact that the HMS will be operating well within its capabilities lead to the expectation that the systematic uncertainty associated with detector acceptances and efficiencies will be around the same 3% level. The extraction of the π^0 yield will have uncertainties from the RCS, *ep*, 2π and η backgrounds, which vary relative to each other for different kinematic settings. In order to estimate the magnitude of the systematic errors arising as a result of contamination from these background sources (as given by the ratios in Table. II,and III), we have relied on the analysis of the RCS collaboration. Since the 2π and η contaminations are small, the major contributions to the uncertainty are from the *ep* and RCS contaminations and are therefore same as those for the RCS experiment. Based on the Monte Carlo simulations an additional 1-5% (depending $N_{2\pi}/N_{\pi}$) uncertainty is assigned due to background from 2π and η (assuming 100% uncertainty in the subraction of this background). A list of systematic uncertainties is shown in Table VI. Most of this description is reproduced from the WACS proposal. The total estimated uncertainty for each of the kinematic settings where the π^0 cross section will be extracted is shown in Table. VII.

3.12. Beam Time Request

A bulk of the beam-time request is just the beam time requested by the WACS proposal. The beam time request for the additional 11 GeV and the 6.6 GeV kinematics is based on time needed to achieve a combined uncertainty of < 10 %. These numbers have been calculated based on the expected rates given in the previous section and include estimated overheads from background measurements without the radiator and configuration changes between kinematic settings. The beam-time estimate for the 4-pass kinematic settings and 5-pass settings are exactly same as

TABLE VI. Table of estimated systematic uncertainties for the π^0 cross section measurement. The total is the quadrature sum.

Source	Uncertainties
	%
Beam charge	1.0
Target thickness	1.0
Bremsstrahlung flux	3.0
NPS efficiency	1.5
HMS efficiency	1.5
HMS tracking efficiency	1.5
RCS background	3.0
$ep\gamma$ background	3.0
$2\pi, \eta$ background	1.0 - 5.0
Total	6.1 - 7.8

those for the WACS experiment (i.e. 425 hrs), since the π^0 data will be collected at the same time as the WACS experiment. The additional beam-time needed for the single 5-pass setting and the 3-pass settings is **56 hours** over the 7 different settings. The net total beamtime request including the common time with the WACS experiment is 481 hrs ($\sim$ 20 day).

3.13. Projected Results

The π^0 photoproduction cross sections measured in this experiment will cover a large range of c.m. energy overlapping with previous measurements at $s < 10GeV^2$,

TABLE VII. Table of estimated total uncertainty (quadrature sum of systematic and statistical) for the each of the kinematic settings where the π^0 cross section will be extracted.

Setting	Uncertainty	Setting	Uncertainty	Setting	Uncertainty	Setting	Uncertainty
	%		%		%		%
5B	8.9	4B	7.6	3A	6.9	3D	7.6
5C	6.7	4C	6.5	3B	7.0	3E	8.1
5D	6.4	4D	6.4	3C	7.3	3F	8.2
5E	6.3	4E	6.5				
5F	7.4						

and extending up $s \sim 20GeV^2$. These results may help resolve the discrepancy between the previous measurements. Fig. 20 shows the projected results at 70°, 90° and 110° c.m. angles.

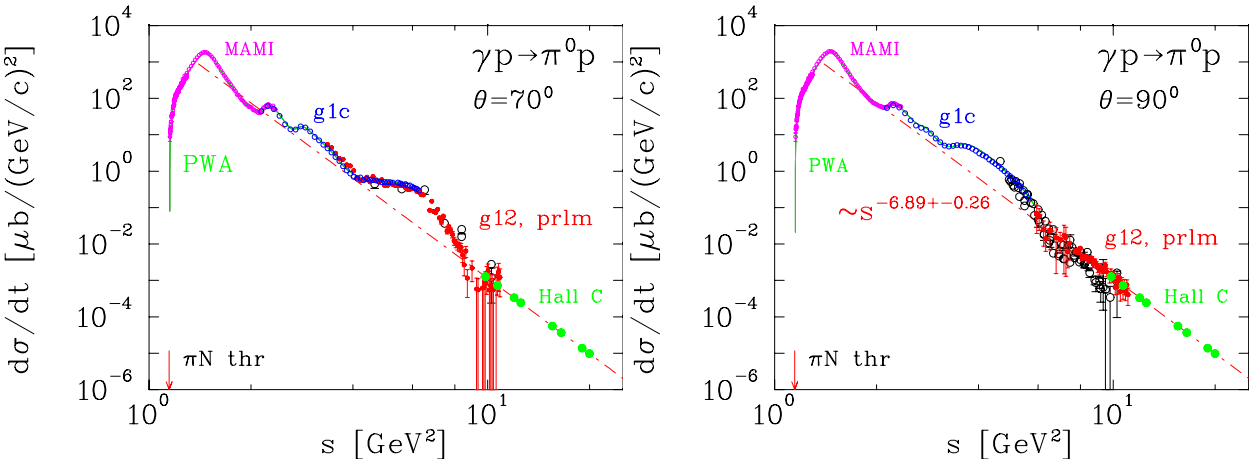

FIG. 19. Projected results at 70° and 90° c.m. angle.

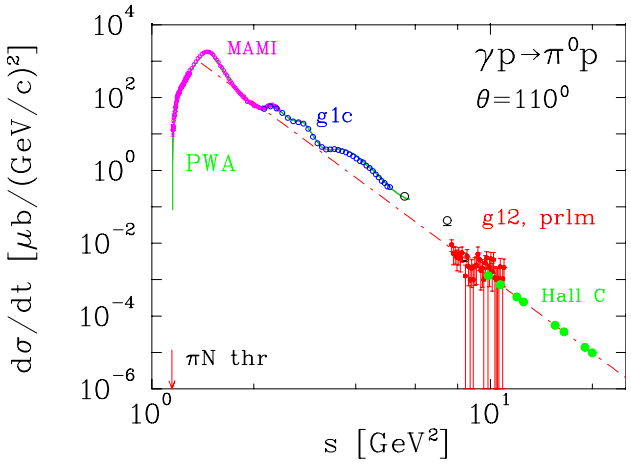

FIG. 20. Projected results at 110°.

4. SUMMARY

The $\gamma p \to \pi^0 p$ process is one of the simplest exclusive processes to investigate the dominance of the handbag mechanism, and to study the onset of scaling behavior for π^0 photoproduction. Utilizing fully the advantages of high luminosity and the energy upgraded CEBAF. The slower decrease of the differential cross-section for the process compared with many other photon induced two-body processes allows differential cross-section measurements all the way to the highest possible center-of-mass energy with a 11 GeV CEBAF beam. Specifically, a 11 GeV beam will allow:

- A precise measurement of the π^0 photoproduction cross section at the highest energies available, to help resolve some of the discrepancies between the previous measurements.
- Detailed investigation of the angular dependent scaling onset will help understand the origin of scaling behavior.
- Investigate the deviations from scaling behavior and oscillations as suggested

by results [24] on charged pions.

---

[1] X. Ji, Phys. Rev. Lett. **78**, 610 (1997); Phys. Rev. D **55**, 7114 (1997); A.V. Radyushkin, Phys. Lett. **B380**, 417 (1996); Phys. Rev. D **56**, 5524 (1997); M. Diehl, T. Feldmann, R. Jakob, P. Kroll, Eur. Phys. J. **C 8**, 409 (1999).

[2] A. V. Radyushkin, Phys. Rev. **D 58**, 114008 (1998) [hep-ph/9803316].

[3] M. Diehl, T. Feldman, R. Jacob, P. Kroll, Eur. Phys. J. **C 8**, 409 (1999) [hep-ph/9811253].

[4] H. W. Huang, P. Kroll, Eur. Phys. J **C 17**, 423 (2000) [hep-ph/0005318].

[5] N. Kivel and M. Vanderhaeghen, JHEP **04**, 029 (2013); arXiv:1212.0683; arXiv:1312.5456.

[6] H. W. Huang, P. Kroll, T. Morii, Eur. Phys. J. C **23**, 301 (2002).

[7] M. Diehl and P. Kroll, Eur. Phys. J. C 73, 2397 (2013); arXiv:1302.4604.

[8] G. Eichmann and C. S. Fischer, Phys. Rev. D 87 , 036006 (2013); arXiv:1212.1761.

[9] H. W. Huang, R. Jacob, P. Kroll, K. Passek-Kumericki, Eur. Phys. J **C 33**, 91 (2004); P. Kroll private communication.

[10] R. Ent, T. Horn, H. Mkrtchyan *et al.*, Neutral-Pion Spectrometer Facility in Hall C, proposal to Jefferson Lab PAC 40.

[11] B. Wojtsekhowski, D. J. Hamilton, S.Širca *et al.*, Wide-angle Compton scattering at 8 and 10 GeV photon energies, proposal to Jefferson Lab PAC 41.

[12] C. White *et al.*, Phys. Rev. **D49**, 58 (1994).

[13] S.J. Brodsky and G.R. Farrar, Phys. Rev. Lett.**31**, 1153 (1973); Phys. Rev. D **11**, 1309 (1975); V. Matveev *et al.*, Nuovo Cimento Lett. **7**, 719 (1973);

[14] G.P. Lepage, and S.J. Brodsky, Phys. Rev. D **22**, 2157 (1980).

[15] T. Gousset, B. Pire and J. P. Ralston, *Phys. Rev.* D **53**, 1202 (1996).

[16] N. Isgur and C. Llewelyn-Smith, Phys. Rev. Lett. **52**, 1080 (1984).

[17] X. Ji, J.-P. Ma and F. Yuan, Phys. Rev. Lett. **90**, 241601 (2003).

[18] J. Polchinski and M.J. Strassler, Phys. Rev. Lett. **88**, 031601 (2002); R.C. Brower and C.I. Tan, Nucl. Phys. B **662**, 393 (2003); O. Andreev, Phys. Rev. D **67**, 046001 (2003).

[19] S. J. Brodsky and G. F. de Teramond, Phys. Lett. **B582**, 211 (2004); S. J. Brodsky *et al.*, Phys. Rev. D **69**, 076001 (2004).

[20] M. Fuchs ıet al., Phys. Lett. **B368**, 20 (1996); R. Beck ıet al., Eur. Phys. J **A 28S1**, 173 (2006).

[21] M. Dugger *et al.*, Phys. Rev. **C76**, 025211 (2007); M. Dugger *et al.*, Phys. Rev. **C79**, 065206 (2009).

[22] M. Kunkel *et al.*, Preliminary (2014).

[23] P. Joos, Preprint DESY-HERA 70-1, (1970).

[24] L. Y. Zhu *et al.*, Phys. Rev. Lett. **91**, 022003 (2003); L. Y. Zhu *et al.*, nucl-exp/0409018.

[25] W. Chen *et al.*, Phys. Rev. Lett. **103**, 012301 (2009).

[26] R. A. Arndt, W. J. Briscoe, R. L. Workman, and I. I. Strakovsky, the GWU CNS Database, http://gwdac. phys.gwu.edu/analysis/pr_analysis.html

[27] A. Sibirtsev, J. Haidenbauer, S. Krewald, T.-S. H. Lee, U.-G. Meissner, and A. W. Thomas, Eur. Phys. J. A 34, 49 (2007); A. Sibirtsev (private communications).

[28] R.L. Anderson *et al.*, Phys. Rev. **D14**, 679 (1976).

[29] "Photoproduction of Elementary Particles", edited by H. Genzel, P. Joos and W. Pfeil pp16-268, (1973).

[30] J. Napolitano *et al.*, *Phys. Rev. Lett.* **61**, 2530 (1988); S.J. Freedman *et al.*, *Phys. Rev.* C **48**, 1864 (1993); J.E. Belz *et al.*, *Phys. Rev. Lett.* **74**, 646 (1995).

[31] C. Bochna *et al.*, *Phys. Rev. Lett.* **81**, 4576 (1998).

[32] E.C. Schulte, *et al.*, *Phys. Rev. Lett.* **87**, 102302 (2001);

[33] P. Rossi *et al.*, Phys. Rev. Lett. **94**, 012301 (2005); M. Mirazita *et al.*, Phys. Rev. C **70**, 014005 (2004).

[34] K. Wijesooriya, *et al.*, *Phys. Rev. Lett.* **86**, , (2)975 (2001).

[35] K. Wijesooriya, *et al.*, *Phys. Rev.* C **66**, , (0)34614 (2002).

[36] W. Luo *et al. Phys. Rev. Lett.* **108**, , (2)22004 (2012)

[37] P. V. Landshoff, Phys. Rev. D **10**, 1024 (1974).
A.W. Hendry, Phys. Rev. D **10**, 2300 (1974).
D.G. Crabb *et al.*, Phys. Rev. Lett. **41**, 1257 (1978).

[38] Q. Zhao and F. E. Close, Phys. Rev. Lett. **91**, 022004 (2003).

[39] A. V. Belitski, X. Ji and F. Yuan, Phys. Rev. Lett. **91**, 092003 (2003).

[40] M. K. Jones *et al.*, Phys. Rev. Lett. **84**, 1398 (2000); O. Gayou *et al.*, Phys. Rev. Lett. **88**, 092301 (2002).

[41] P. Degtiarenco private communication.

[42] M. Kubantsev *et al.*. Performance of the Primex Electromagnetic Calorimeter, arxiv:physics/0609201, Sept 22, 2006; A. Gasparyan, Performance of PWO crystal detector for a High Resolution Hybrid Electromagnetic Calorimeter at Jefferson Lab, Proceed. X Int. Conf. on Calorimetry in Particle Physics, Perugia, Italy, 29 March - 2 April 2004, pp 109.

[43] David J. Hamilton, A simulation of the 12 GeV Hall C RCS experiment, University of Glasgow, April 14, 2013 (unpublished).

[44] Ren-yuan Zhu, Nucl. Instr. Meth. A 613 (1998) 297

[45] C. Hyde-Wright, A. Nathan, and B. Wojtsekhowski, spokespersons, JLab experiment E99-114.

[46] P.E. Bosted, Phys. Rev. C 51 (1995) 409.

[47] The Durham HepData Project; http://hepdata.cedar.ac.uk/reaction

5. APPENDIX A

Update to Jefferson Lab PAC 42

Neutral Particle Spectrometer (NPS) Facility in Hall C

June 1, 2014

A. Camsonne, R. Ent, P. Nadel-Turoński, S. A. Wood, B. Wojtsekhowski, C. Zorn
Jefferson Lab, Newport News, VA 23606

A. Asaturyan, A. Mkrtchyan, H. Mkrtchyan, V. Tadevosyan, S. Zhamkochyan
A.I. Alikhanyan National Science Laboratory, Yerevan 0036, Armenia

M. Guidal, C. Munoz Camacho, R. Paremuzyan
Institut de Physique Nucleaire d'Orsay, IN2P3, BP 1, 91406 Orsay, France

I. Albayrak, M. Carmignotto, N. Hlavin, T. Horn[1], F. Klein, B. Nepal, I. Sapkota
The Catholic University of America, Washington, DC 20064

C. Hyde, M. N. H. Rashad
Old Dominion University, Norfolk, VA 23529

P. King, J. Roche
Ohio University, Athens, OH 45701

D. Day, D. Keller, O. Rondon, J. Zhang
University of Virginia, Charlottesville, VA 22901

J. R. M. Annand, D. J. Hamilton
University of Glasgow, Glasgow, Scotland, UK

S. Širca
University of Ljubljana, Ljubljana, Slovenia

D. Dutta
Mississippi State University, Starkville, MS 39762

[1] Contact person: hornt@jlab.org

Contents

1 Introduction

The Neutral Particle Spectrometer (NPS) is envisioned as a facility utilizing the well-understood HMS and the infrastructure of the SHMS to allow for precision (coincidence) cross section measurements of neutral particles. It can be canelevered off the SHMS carriage covering detection angles between 5.5 and 30 degrees, and be positioned on top of the SHMS carriage to cover angles between 25 and 60 degrees. The NPS will be used as photon detector for an approved Deeply-Virtual Compton Scattering [1] experiment, E12-13-010, that aims to extract the real part of the Compton form factors without assumptions. It will also be used as neutral-pion detector for π° electroproduction in semi-inclusive Deep-Inelastic Scattering, in approved experiment E12-13-007, to validate our basic understanding of the partonic interpretation of these reactions with several experimental advantages as compared to likewise charged-pion reactions [2]. Here, the neutral pion will be detected by measurement of its $\gamma\gamma$ decay products.

The NPS could further be used as photon detector for Wide-Angle Compton Scattering [3, 4] reactions, and as neutral-pion detector for exclusive π° photoproduction [5], proposals submitted to this PAC.

The basic concept for the NPS is a highly segmented electromagnetic calorimeter preceded by a compact sweeping magnet. The experiments it enables require detection of neutral particles with energies ranging between ≈ 1 and ≈ 8 GeV, with good energy resolution (1-2%), and good coordinate (2-3 mm) and angular (0.5-1 mr) resolution, comparable to the resolutions of the focusing spectrometers in Hall C. The neutral particle scattering angles cover 6.7-25 degrees for the approved program, and up to 60 degress for the foreseen program. The distance of the calorimeter from the target ranges from 3 to 12 meters. As an example, the minimum angle of the approved program at a distance of 4 m is 7.2°.

The NPS is an efficient and economical way to meet all of the presently known experimental requirements. It will consist of the following components:

- $PbWO_4$ crystals in a temperature controlled frame;
- a set of high voltage distribution bases with built-in amplifiers [6] for operation in high-rate environments;
- essentially deadtime-less digitizing electronics to independently record the pulse amplitudes from each crystal;
- a sweeping magnet of roughly 0.3-0.6 Tm;
- a cantelevered platform of the SHMS carriage to allow precise, remote rotation around the Hall C pivot over an angular range between 5.5 and 30 degrees;
- a platform to mount the NPS on top of the SHMS carriage to allow precise, remote rotation around the Hall C pivot over an angular range between 25 and 60 degrees;
- a light monitoring and curing system to monitor and restore crystal optical properties.

A more detailed description of the NPS facility is in a document submitted to PAC40 [7]. In this update document we will highlight present planning, and progress and results from some of our studies on the critical components of the calorimeter, leading towards a small prototype. We will present some of the results from our studies on LEDs used for gain monitoring and possible curing, phototube sensitivity to infrared light, plans for crystal irradiation and curing tests, as well as details and progress of assembly of the prototype and its LED curing system.

2 NPS Calorimeter

The NPS calorimeter will consist of an array of up to 1116 scintillating $PbWO_4$ and up to 208 PbF_2 crystals, covering a solid angle of 25 msr at a distance of 4 m from the target. In general, the NPS requires crystals with high transparency, high light yield, good timing where 90% of the light is emitted within 30-50 ns, and good radiation hardness. Also important are crystal geometry and integrity.

In the ideal case, the NPS calorimeter will consist of a set of brand new $PbWO_4$ crystals. Taking advantage of the existing $PbWO_4$ crystals (and accompanying photomultiplier tubes (PMTs)) of the high-resolution inner part of the Hybrid Electromagnetic Calorimeter (HYCAL) [8] used for the PrimEx/PrimEx-II experiments, one arrangement is an assembly of 1080 $PbWO_4$ crystals in a 36 by 30 matrix. Our goal is to acquire new $PbWO_4$ crystals, both to allow flexibility of scheduling of experiments at Jefferson Lab (given that more and more experiments plan to use $PbWO_4$ crystals) and to increase radiation hardness. Nonetheless, given the worrying lack of qualified vendors of $PbWO_4$ crystals in the world, and to evade scheduling conflicts, we investigate an alternate arrangement consisting of $\approx$ 600 $PbWO_4$ crystals and the available 208 PbF_2 crystals from the Hall A DVCS calorimeter, to complete a calorimeter with similar solid angle. The 600 $PbWO_4$ and $\approx$200 PbF_2 crystals would provide a hybrid calorimeter configuration. A similar but not identical hybrid calorimeter was succesfully used in the PrimEx HYCAL calorimeter, which had an inner core of $PbWO_4$ and an outer ring of lead glass crystals.

2.1 Choice of Crystals

Analysis of general properties of heavy crystals used in calorimetry show that BGO, $PbWO_4$, PbF_2 and LSO/LYSO are among the candidates. BGO is a commonly used scintillation crystal with a timing property of 300 ns, and is not suitable for the NPS calorimeter. LSO/LYSO crystals have acceptable timing properties, but do not provide an economically favorable option as they would be prohibitively expensive for our envisioned sizes.

Both $PbWO_4$ and PbF_2 crystals are fast, 5-14 ns for $PbWO_4$ and $<$30 ns for PbF_2, and are suitable for experiments requiring fast signals with short tails to minimize pile-up at high rates. This choice is of course also dictated by availability of these type of crystals used in JLab DVCS and PrimEx experiments.

Since the NPS calorimeter may by necessity perhaps be a combination of $\sim$600 $PbWO_4$ blocks (from PrimEx) and 208 PbF_2 blocks (from Hall A DVCS), the component studies

should be optimized to include this possibility. This includes taking into account that for $PbWO_4$ crystals the mechanism of light emission is pre-dominantly scintillation, while it is pure Cherenkov radiation for PbF_2. The difference in dimensions and optical properties of $PbWO_4$ and PbF_2 crystals may similarly require different intensity for light monitoring.

2.2 Crystal Transmittance Measurements

One obvious question that needs addressing for a hybrid calorimeter is if we could use a single primary light source for both $PbWO_4$ and PbF_2 crystals. Hence, we first have to know the transmittance of light for both types of crystals.

We measured the transmittance of $PbWO_4$ and PbF_2 crystals using an existing setup of Jefferson Lab's Radiation Detector and Imaging group, in the ARC. The results are shown in Fig. 1. Comparison of the transmittance curves illustrates that $PbWO_4$ and PbF_2 crystals are very similar in the region above λ ~400 nm, even if different in the short wavelength region (λ ~250-350 nm). Hence, for instance blue light with a wavelength ~470 nm should be acceptable for both types of crystals as a common light source for a monitoring system.

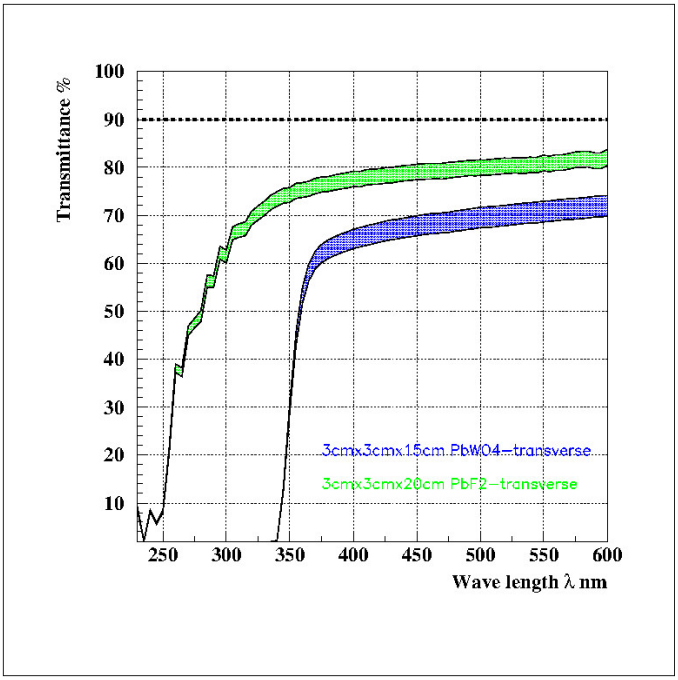

Figure 1: Light Transmission efficiencies of the PbF_2 (green) and $PbWO_4$ (blue) crystals (3.0 cm thickness) versus light wave length. Color bands represent spread in data measured at different points of the crystals.

Note that the output pulse timing and shape for the crystals will be different. It would be preferable to use the same digital filtering for actual physics events and light pulser events, but if this difference is significant it may require a different digital filtering.

3 Curing System and Component Studies

All known crystals suffer from radiation damage. The most common damage phenomenon is radiation-induced absorption (reduction in crystals light attenuation length). Previous studies show that the $PbWO_4$ crystal scintillation mechanism is not damaged up to a radiation dose of 2.2 Mrad. Radiation damage of the crystals themselves show a clear saturation, and both transmittance and light yield are stabilized after an initial dosage of a few tens to 50-100 krad, with the level of damage at saturation being dose dependent. Naturally, the radiation damage will depend on the chemical composition of the crystals, and the type and amount of the dope material.

Studies of the radiation conditions in Hall C show that during the planned experiments the accumulated radiation dose may well exceed 100-200 krad, especially for small-angle operation of NPS. To keep the calorimeter performance at the required precision level of understanding efficiency and resolution, we plan to develop a light curing system, and periodically use this between different kinematic settings of the experiments, or whenever the accumulated dose will reach $\sim$50 krad.

3.1 General Concepts of Curing System

To restore the crystal optical properties, a curing system will be developed with as minimum impact on the running of the experiments. Our baseline method is to use blue light of wave length between 400 and 500 nm for so-called optical bleaching. It is well established that blue light is most effective in removing the radiation damage and resetting the crystal's attenuation length. The required light intensity is of an order of 1-2 mW/cm^2, and thus for the NPS 20×20 mm^2 ($PbWO_4$) or 30×30 mm^2 (PbF_2) crystals we need a curing system with power of 5-10 mW/crystal. Standard curing with blue light can be very effective: nearly 90% of the original signal can be restored within first 200 minutes with a photon flux of $\sim 10^{16}$ γ/s. However, the technique is invasive (requiring turning PMTs off and Hall access), and based on experience with the Hall A/DVCS experiment can affect PMT operation.

Thus, we also plan to study a curing system with permanent infrared illumination based on those from, *e.g.*, Refs. [9, 10]. Studies show that at such longer wavelengths (600-1000 nm) a significant recovery is possible, but for a long time of irradiation. This is proven to work very well for low doses ($\sim$3 krad) and can be operated remotely without access to the experimental area. The main difficulty of this method is the lower efficiency, by a factor of 20-50 relative to blue light, which then must be compensated by an increase of the light intensity (up to $\sim 10^{16}$ photons/s per block).

We plan to design, build and test both systems, based on blue and on permanently installed super bright infrared light ($\lambda \geq$940 nm). To be compatible with the NPS, they will have similar mechanical design. For both the curing and the light monitoring systems, detailed studies and selection of the most effective Light Emitting Diodes is critical.

3.2 Selection of Blue and Infrared LEDs

It is important to select LEDs that can withstand ∼1 Mrad or higher radiation doses without significant degradation (radiation hard LEDs). This strongly depends on the material used in LED production. The best radiation hardness are shown by LEDs based on SiC, GaN and AlGaInP (see [12, 13] and references there). Radiation hardness of the LEDs has been tested with protons, neutrons and photons. It was shown that for GaAs-based LEDs the normalized light output drops by factor ∼5 after radiation doses of 5×10^8 - 10^{10} p/cm^2 caused by protons or neutrons, the degradation effect from photons is 100-1000 times lower: for an accumulated dose of ∼1 kGy (∼100 krad) from photons no noticeable change in the light output or timing characteristics of GaAs-based LEDs was observed.

3.2.1 Infrared LED Studies

We have used a test setup of the Radiation Detector and Imaging Group to measure the absolute intensity of several types of blue (RL5-5515, RL5-4630 and SLA-580BCT3F) and infrared (NIR LD-274-3 and TSAL7400) LEDs. Some details of the setup are shown in Fig. 2. The infrared LED (seen on the left) is mounted on a special support structure. The calibrated Photodiode S2281 (seen on right) with an effective area of 100 mm^2 and quantum efficiency of ∼ 67% (at λ ∼950 nm) measures intensity of the emitted light (its current is nearly linearly proportional to the LED intensity). The distance between LED and Photodiode can be varied from 0.5 cm to 20 cm. The LED driving current is measured by a FLUKE multimeter and the Photodiode current is measured by high accuracy KEITHLEY picoamperemeter.

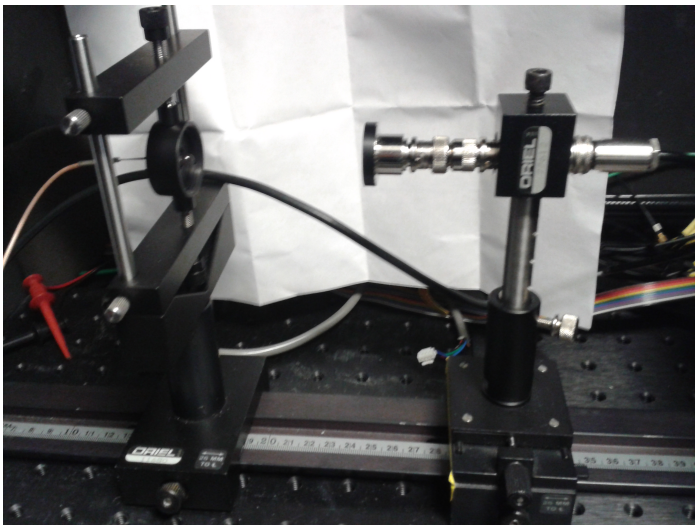

Figure 2: LED test setup. An infrared LED (on the left) is mounted on a special support structure. The calibrated Photodiode S2281 (on the right) with an effective area of 100 mm^2 measures the intensity of the emitted light. The distance between LED and Photodiode can be varied from 0.5 cm to 20 cm.

All equipment is installed in a *mini-dark-room*. With closed doors the photodiode dark current, with LED OFF was on the level of ∼0.001 nA. With the doors open the dark current value jumped to 1.1 μA (about 1000 times higher). Though all the LED studies were done with closed doors, this value of dark current is so small that one could do measurements with the doors open.

The electronic circuit which drives the LED used a fixed 5.0 V of the power supply. The value of the LED driving current was then changed over the range from 0 to 100 mA by changing the value of a 1 kΩ variable resistor. We then measured the LED emission intensity versus this driving current with the photodiode located at distances of both ∼3 cm and ∼7 cm from the LED. Results for both infrared LEDs are shown in Fig. 3.

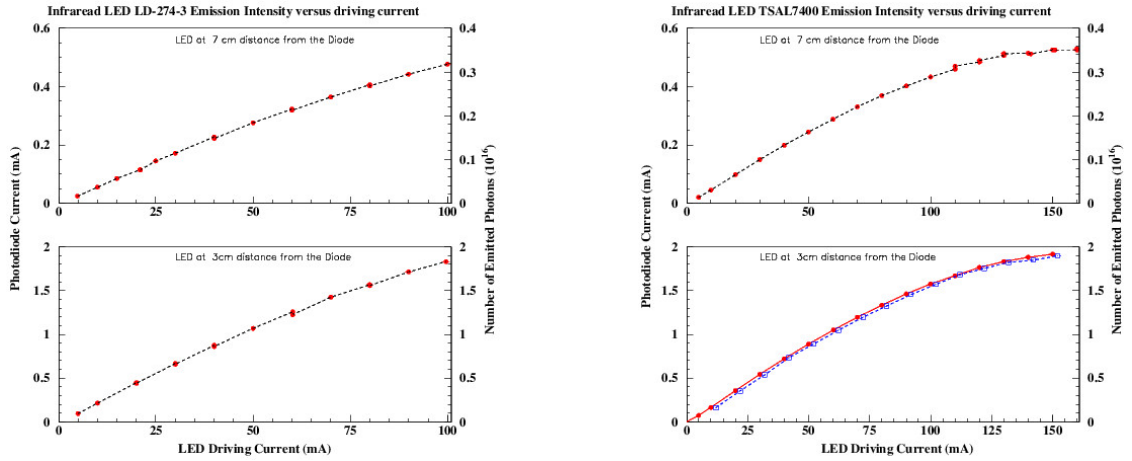

Figure 3: Emission intensity of the Infrared LED LD-274-3 (left) and TSAL7400 (right) versus driving current at distance 7 cm (top) and 3 cm (bottom).

At a distance of ∼3 cm, where the LD-274-3 LED fully illuminates the calibrated photodiode (with an effective area of 100.0 mm^2) the energy output is equivalent to 2×10^{16} $\gamma/sec/cm^2$.

The wavelength of the LD-274-3 LED is λ=950 nm at the peak intensity. Using this number as an average to estimate energy of the photons, one obtains an equivalent energy of 1.3 eV:

$$E_\gamma = h \times \nu = h \times c/\lambda = (6.63^{-34}\ m^2 kg/s \times 3 \times 10^8\ m/s)/(950 \times 10^{-9}\ m) \approx 1.31\ eV. \quad (1)$$

A photon flux $N_\gamma = 2 \times 10^{16} \gamma/s$ will then deposit a power of $P_\gamma = N_\gamma \times E_\gamma = 2 \times 10^{16} \times 1.31\ eV/s \approx 4.2\ mW$ per cm^2 (at a mean wavelength of 950 nm and at a nominal maximum current of 100 mA driving the LED, as listed in the Osram data sheet).

The data show that the emission intensity is almost linear with driving current. Beyond 60 mA, the output begins to curve slightly indicating the onset of saturation of the emission intensity of the LED. We verified that this saturation is due to the LED and not the photodiode by doing additional measurements with attenuation of the LED light output, by installing neutral density filter with attenuation factor of 9.25 in front of the LED. The data without filter and with filter, when scaled by the attenuation factor, are in good agreement.

3.2.2 Blue LED studies

The same experimental setup and the same technique were also used to study the emission intensity of several types of blue LEDs, as a function of both the driving current and the distance from the photodiode. Data for a distance of ∼3 cm are shown in Figs. 4 and 5.

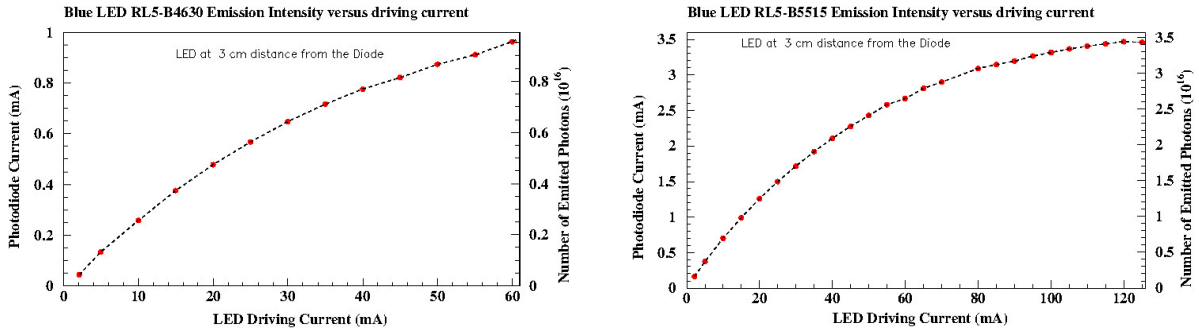

Figure 4: Emission intensity of the Blue LED RL5-B4630 (left) and RL5-B5515 (right) versus driving current at a distance of 3 cm.

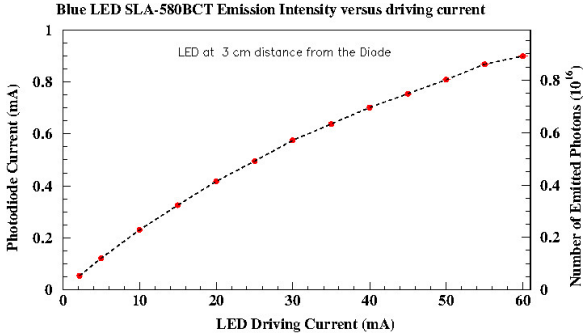

Figure 5: Emission intensity of the Blue LED SLA-580BCT versus driving current at a distance of 3 cm.

3.3 R4125 phototube sensitivity to Infrared light

The main limiting factor for the IR LED based curing system for the NPS can be the small yet remaining PMT sensitivity to infrared light. It is assumed that IR LED curing would be conducted continuously during the experiment without interruption of data taking with the PMT high voltage ON. For such a requirement it is crucial to know:

- at what level the continuous use of an IR LED will change the PMT anode current, and
- if this rise of anode current will have a negative impackt on the PMT linearity, gain, and lifetime.

For all types of PMTs operating in a high background condition (with high rate and/or high anode current) the limiting factors are the lifetime of the photocathode and the gain. Photocathode lifetime is defined by the amount of charge passing between the photocathode and the first dynode after which the PMT quantum efficiency drops by factor ∼2 from its nominal value. The PMT gain-lifetime is defined by amount of total charge passing through anode which results degradation of the PMT gain by a factor of two.

CMS studies show that after some amount of charge collection the PMT characteristics, apart from the gain, do not show any significant change from their values at the start of the measurement: in Ref. [15] the results of a complete test of 2000 Hamamatsu R7525HA phototubes for the CMS forward hadron calorimeter are reported. This is an 8-stage PMT with 25 mm diameter of Bialkali photocathode, with gain $\sim 5 \times 10^5$ at high voltage 1750 V, and typical anode dark current of 5 nA (maximum ∼100 nA). The studies found that the relative drop in the gain after 3000 C of charge collection depends on the High Voltage (or gain) and may vary from ∼2 (at low HV) to 5 (at high HV).

In general, pending on the type of PMT, the photocathode and dynode materials, the mechanical construction and the operation regime, the photocathode-lifetime may well vary from a few tens to a few hundred mC, while the gain-lifetime may vary from few hundred to few thousand C. As a consequence, to prolong the PMT lifetime one needs to keep the cathode and anode currents as low as possible. This is also required for as minimum as possible dark currents of the PMT. Any additional source which may increase the PMT anode current (dark current) will have a negative impact on the lifetime of the PMT. Thus, curing of the crystals in situ by using a high-intensity infrared light without turning the phototube high voltages off is in practice only possible if the rise of the PMT dark current when the infrared LED is on is completely negligible relative to the anode current, or less than a few times of the nominal dark current.

The possibility to perform continuous curing of the crystal in-situ (with the PMTs' HV on) using infrared light with wavelength $\lambda \geq$900 nm depends thus on the (quantitatively unknown) quantum efficiency of the PMT in this wavelength region. Since effective curing will require a very high IR light intensity ($\geq 10^{17}$ γ/sec) this is even an issue for a small quantum efficiency this IR wave lenght: the phototube could still be completely damaged with such a high intensity IR light.

We thus measured the R4125 phototube's sensitivity to the infrared light. The tube was installed on front of the LED. The measurements were done at different driving currents of the LED (from 0 up to 100 mA), at distances of 0.5 cm and 16 cm (18 cm), with and without a PbF_2 ($PbWO_4$) crystal placed in front of the PMT, and at different gains of the PMT. For these measurements we used one of the prototypes of the active divider with built-in amplifier we developed earlier for this PMT, to increase linearity up to high rates. In the measurements, we first measured single electron peak and gain of R4125. At high voltages of 1600, 1700 and 1750 V, respectively, we found the following gain values: 3.8×10^7; 7.6×10^7 and 1.0×10^8. These values are much higher than those listed in the Hamamatsu data sheet (gain of 10^5 at 1500 V) due to the use of the active divider.

To measure the PMT quantum efficiency at wavelengths far beyond the sensitivity range specified in the Hamamatsu data sheet, in the infrared, the output signal was sent to an ADC, and we used a simple DAQ system based on Lab-VIEW. The ADC gate width was

set to be 150 nsec, and a channel was equivalent to 100 fC. Data for each setting were taken for 5 min (300 sec) with a frequency of ∼200-300 Hz. Amplitude distributions of the signals were detected at different driving currents through the IR LED LD-274-3 and TSAL7400 type LEDs. We then repeated the measurements with a crystal (PbF_2 or $PbWO_4$) installed between the LED and the PMT, as shown in Fig. 6.

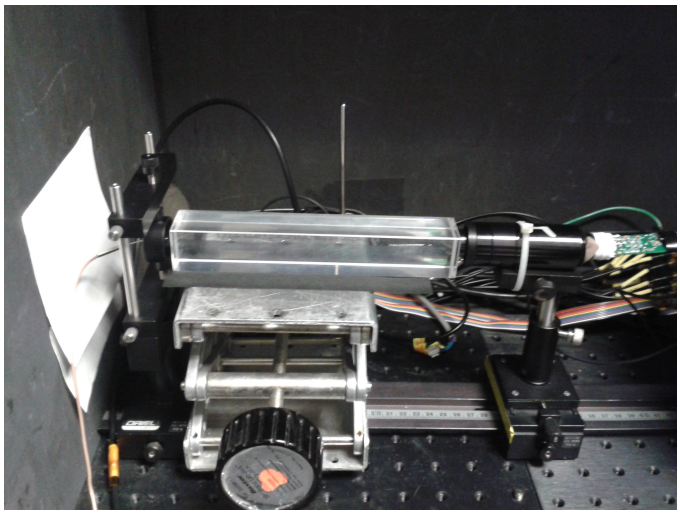

Figure 6: Experimental setup for the PMTs sensitivity measurements to infrared light. A 20 cm PbF_2 crystal is installed between the PMT and the LED.

The data suggest that PMT R4125 has a very low, yet not negligible, quantum efficiency relative to infrared light. As example, we show in Fig. 7 the amplitude distributions of the signals detected by the R4125 PMT at different values of the driving currents of the infrared LED NIR LD-274-3. It is possible that the PMT sensitivity may be due to contamination by short wavelength light of the IR LED spectrum. Tests were thus repeated with a 900 nm filter cutting all wavelengths but IR. No difference between the measurements with and without filter were found. This suggests that the majority of the light has IR wave length, that the PMT has a non-zero efficiency with respect to IR light, and that the PMT could thus potentially receive long-term damage if left on during *in situ* IR curing. More studies are ongoing, for instance given the sensitivity to wavelengths $\lambda \geq$900 nm, we may also search for suitable LEDs with an emission spectrum >1000 nm.

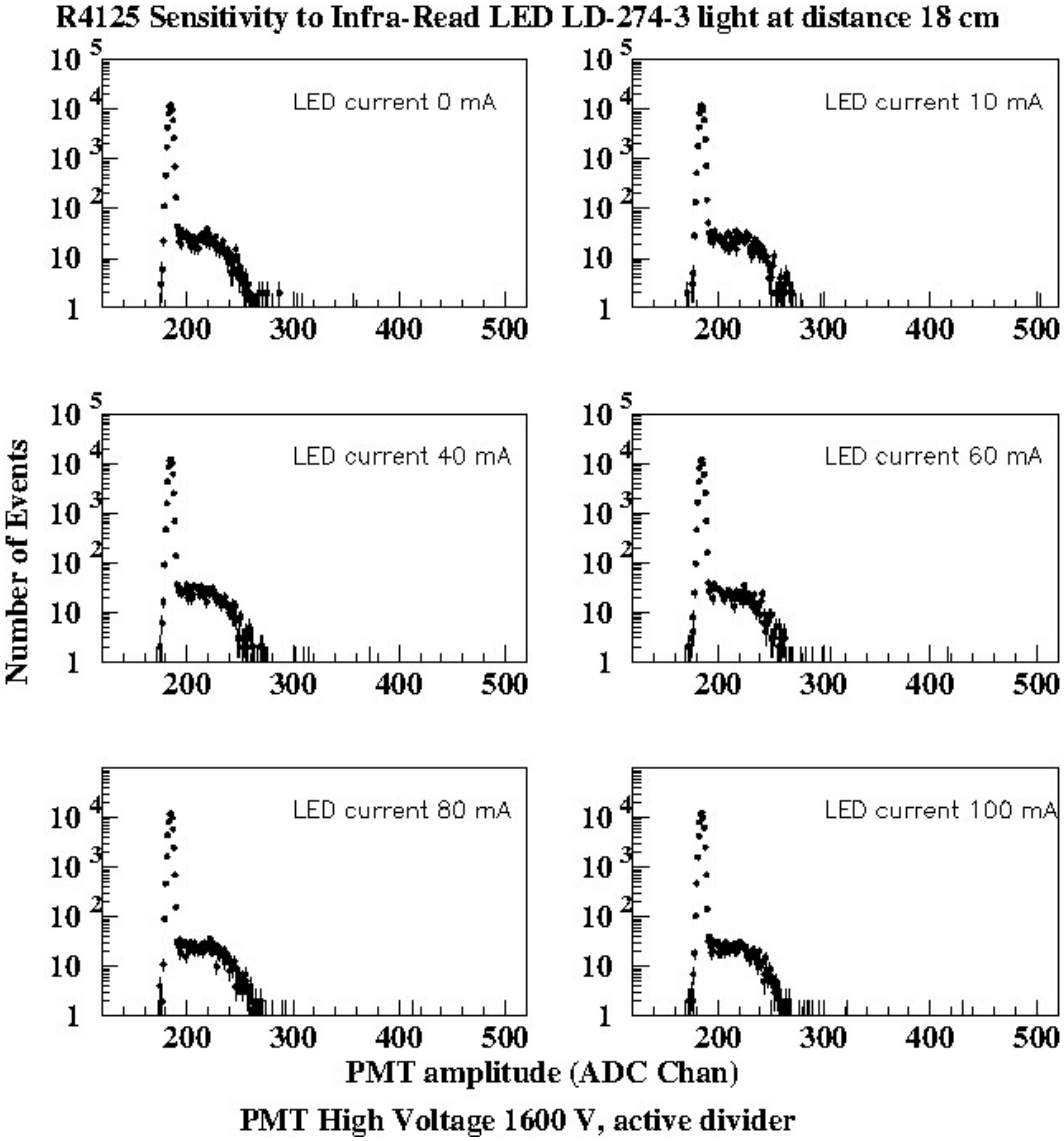

Figure 7: The amplitude distributions of the signals detected by PMT R4125 at different values of infrared LED NIR LD-274-3 driving currents.

To start studying potential damage of the PMT during long-term operation, we measured the PMT R4125 anode current versus driving current of IR LEDs LD-274-3 with the PMT at high voltage settings of 1400 V, 1500 V and 1600 V, respectively, when a single IR LED or a matrix of four IR LEDs illuminated the photocathode. Some results of the measured anode currents with the PMT set at a high voltage of 1600 V are shown in Fig. 8.

With the high voltage of the PMTs on, and no LED driving current, the dark current of the PMT is 11 nA for 1400 V, 18 nA for 1500 V and 28 nA for 1600 V, respectively. Then, for the case where a single LED is positioned at a distance of 19 cm of the front of the PMT, and an LED driving current of 50 mA, the anode current is 309 nA for 1400 V, 492 nA for 1500 V and 758 nA for 1600 V, respectively. For reference, for a similar 50 mA driving current and a matrix of four IR LEDs at this distance, the photon flux would be

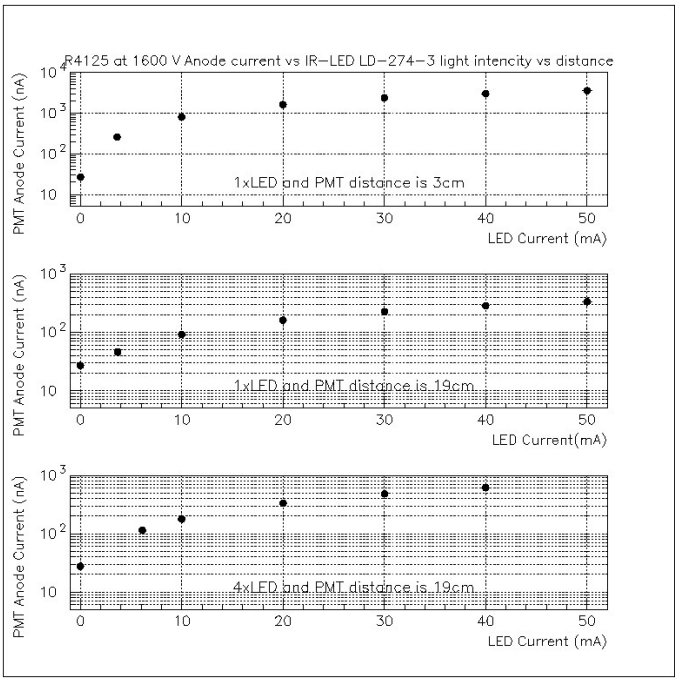

Figure 8: PMT anode current, at a high voltage setting of 1600 V, versus the driving current of IR LEDs: (top)- use of one LED positioned at distance 3 cm from the PMT; (middle)- similar, at a distance of 19 cm from the PMT; and (bottom- a matrix of four LEDs at a distance of 19 cm from the PMT

.

$\sim 10^{17}\ \gamma/cm^2$/sec. This corresponds to a total charge passing through the PMT due to dark currents of only ∼3C, for a 1000 hour run (at a high voltage of 1600 V).

The maximum anode current for the R4125 PMT is ∼0.1 mA. The gain of the PMT, using the active divider (with amplifier), is $\sim 3.8 \times 10^7$ at a high-voltage setting of 1600 V. Most likely we will only require a gain in the 10^5 gain range, and not use high voltage settings higher than 1400-1500 V. Thus, there may not be an adverse effect on the PMT, yet it is clear that more study is needed. For the distance of 19 cm, close to the anticipated geometry using ∼18 cm $PbWO_4$ crystals or ∼20 cm PbF_2 crystals sandwiched between the PMT and LED, the PMT dark current values are listed versus the LED driving current in Table 1.

4 Further Studies and Prototyping

4.1 Design and construction of the curing system

For further tests we plan to make two versions of the curing system. In the first version, the curing will be performed with a matrix of 4 ultra-bright Blue LEDs per block (with intensity about $10^{16}\ \gamma$/sec per block). The second version would be a clone of the first one, but with a matrix of 4 ultra-bright Infra-Red LEDs per block (with intensity about $5 \times 10^{17}\ \gamma$/sec

Table 1: R4125 phototube anode dark current at an operating high voltage of 1600 V versus the LD-274-3 driving current. The left half of the table illustrates the case when using a single LED, the right half for the case of using a matrix of four LEDs. In each case the PMT was located at a distance of 19 cm from the LED(s).

I_{LED} (mA)	I_{Anode} (nA)	I_{LED} (mA)	I_{Anode} (nA)
0.0	27	0.0	27
3.7	46	6.0	114
10.0	92	10.0	177
20.0	161	20.0	334
30.0	225	30.0	478
40.0	284	40.0	609
50.0	332	53.0	758

per block). In each case, the matrix of ultra-bright LEDs will be mounted at small distance from the crystals. In Fig. 9 we shown a partly assembled prototype curing system.

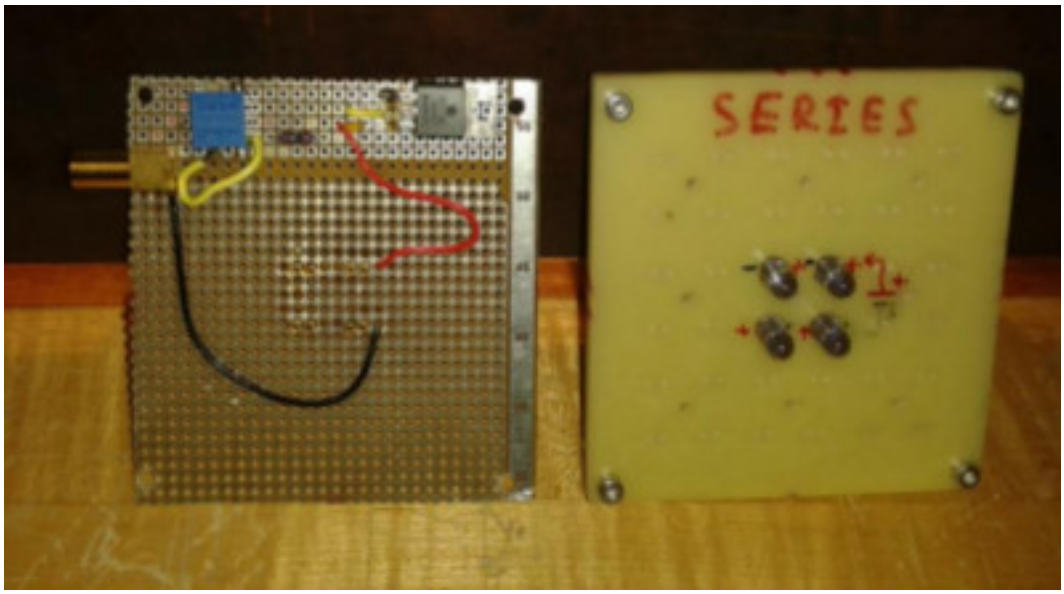

Figure 9: Partly assembled Infrared LED curing system.

4.2 Irradiation of the $PbWO_4$ crystals

We further plan to do controlled irradiation and curing studies of the various crystals. To this end, we plan to use four $PbWO_4$ crystals, each with dimensions $\sim 1.5 \times 1.5 \times 2.0\ cm^3$ for radiation tests. Three of these crystals are passed on to the Jefferson Lab Radiation

Control group who have a small facility that can provide controlled doses with a ^{137}Cs gamma source. We plan to irradiate with up to ∼20 krad dose each step. The fourth crystal will serve as a reference in the measurements. One of the radiated crystals will be used for tracing spontaneous recovery with time, the two others will be used for curing studies with blue and infrared lights. We plan to monitor the curing effect by intermittent light transmission measurements of the crystals. This work has just started.

4.3 Prototype Design

Taking into account the possibility of construction of the NPS calorimeter as a combination of $PbWO_4$ and PbF_2 crystals, we have designed a prototype frame that could include both scenarios: a matrix of 3 by 3 $PbWO_4$ crystals, and a matrix for the $PbWO_4$/PbF_2 hybrid case (3 by 2 $PbWO_4$ crystals and 2 PbF_2 crystals. We plan to again use the 19 mm diameter R4125 Hamamatsu PMTs as used in the PrimEx hybrid calorimeter, with our active dividers. We have acquired 10 $PbWO_4$ crystals from SICCAS for our prototype, with quality close to the $PbWO_4$ crystals used by CMS.

4.4 The Light Monitoring system

A light monitoring system will measure variations of the transmittance of crystals in the course of experiment and provide calibration *in situ*. It will be used to control stability of the detector, degradation of the crystals due to accumulated radiation and define condition when curing of the crystals is needed. It will periodically inject light into the detector modules between the real events during data taking, or during special calibration runs with a frequency 10-20 Hz.

There are three important factors which must be taken into account when considering a light source for the system. First, the source should be as stable as possible. The reference photodiode coupled to it will take out pulse-to-pulse instabilities, but it is still useful to have the primary light source stable in short and long time scale. The second factor is light intensity. Intensity of the light delivered to the large number of crystals in the calorimeter must have an equivalent energy of around 1-3 GeV in each of the crystals. The third factor is timing distribution of the pulses. It must be similar to that from the real event (scintillation pulse for $PbWO_4$ and Cherenkov pulse for PbF_2).

We are studying an LED-based monitoring system to control the status of the $PbWO_4$ blocks and the PMT gains in the course of experiments. The light source is an assembly of NICHINA Super Bright NSPB500AS LEDs located outside of the prototype in radiation safe area. Light from this LED assembly will mix and be delivered to the prototype by ~ 200 μm fiber. There is a special ST type optical fiber connecter on the prototype frame for to plug this primary fiber.

Inside of the prototype box this light will split and delivered to each crystal by bandle of fibers: one monitoring fiber per block. One end of all fibers will be bound together and fed into the ST connector, the second end of the fibers will plug into a hole of an envisioned led-holder plate.

References

[1] E12-13-010, Exclusive Deeply-Virtual Compton and Neutral Pion Cross Section Measurements in Hall C, Approved by Jefferson Lab PAC40, C. Munoz-Camacho, R. Paremuzyan, T. Horn, J. Roche, and C. Hyde, spokespersons.

[2] E12-13-007, Measurement of the Semi-Inclusive π° Production as Validation of Factorization, Approved by Jefferson Lab PAC40, T. Horn, R. Ent, H. Mkrtchyan, V. Tadevosyan, spokespersons.

[3] Wide-Angle Compton Scattering at 8 and 10 GeV Photon Energies, Deferred proposal by PAC40, updated proposal submitted to PAC42, D.J. Hamilton, S. Sirca and B. Wojtsekhowski, spokespersons.

[4] Initial State Helicity Correlation in Wide Angle Compton Scattering, Proposal submitted to PAC42, D. Day, D. Keller and J. Zhang, spokespersons.

[5] Large Center-of-Mass Angle, Exclusive Photoproduction of π° Mesons at Photon Energies of 5-11 GeV, LOI12-13-003 submitted to PAC40, proposal submitted to PAC42, D. Dutta, H. Gao, M. Amaryan, S. Sirca, I. Strakovsky, spokespersons.

[6] V. Popov, H. Mkrtchyan, New potomultiplier active base for Hall C Jefferson Lab Lead Tungstate Calorimeter, NSSS2012-1098.

[7] Neutral Particle Spectrometer Facility in Hall C, NPS collaboration, https://hallcweb.jlab.org/experiments/PAC40/

[8] M. Kubantsev et al., Performance of the Primex Electromagnetic Calorimeter, arXiv:physics/0609201, 22 Sept. 2006; A. Gasparian, Proceed. X Int. Conf. Calorimetry in Part. Phys., Perugie, Italy, 29 March-2 April 2004, pp. 109-115

[9] M. Anfreville et al., Nucl. Instrum. Meth. A**594**, 292 (2008).

[10] R.W. Nowotny, PANDA Collaboration, IEEE-2009-05402124.

[11] R. Zhu, L. Zhang, Quality of Mass-Produced Lead Tungstat Crystals, IEEE Transact. on Nucl. Science, 51 (2004) 1777-1783

[12] Characterization of Proton Damage in Light-Emitting Diodes, A. H. Johnston and T. F. Miyahira, IEEE Trans. Nuclear Science 47 (2000) 2500-2507

[13] Energy Dependence of Proton Damage in AlGaAs Light-Emitting Diodes, R. A. Reed et al., IEEE Trans. Nuclear Science 47 (2000) 2492-2499

[14] A Precision Measurement of the Neutral Pion Lifetime via the Primakoff Effect, PrimEx Conceptual Design Report, Primex Collaboration, Jefferson Lab, March 3, 2000

[15] Complete Tests of 2000 Hamamatsu R7525HA phototubes for the CMS-HF Forward Calorimeter, U. Akgun et al. Nucl. Instr. Methods, A 550 (2005) 145-156